Assessment of landscape-scale fluxes of carbon dioxide and methane in subtropical coastal wetlands of South Florida

Erin R. Delaria[1,2,3] , Glenn M. Wolfe[1], Kaitlyn Blanock[4], Reem Hannun[4]† , Kenneth Lee Thornhill[5,6], Paul A. Newman[1], Leslie R. Lait[1,7], S. Randy Kawa[1], Jessica Alvarez[8], Spencer Blum[8], Edward Castañeda-Moya[9], Christopher Holmes[8], David Lagomasino[10], Sparkle Malone[11], Dylan Murphy[8], Steven F. Overbauer[9], Chandler Pruett[8], Aaron Serre[8], Gregory Starr[12], Robert Szot[8], Tiffany Troxler[13], David Yannick[12], Benjamin Poulter[14]

[1]Atmospheric Chemistry and Dynamics Laboratory, NASA Goddard Spaceflight Center, Greenbelt, MD, 20771, USA. [2]NASA Postdoctoral Program, Oakridge Associated Universities, Oak Ridge, TN, 37831. [3]Earth System Science Interdisciplinary Center, University of Maryland, College Park, MD 20740. [4]Department of Geology and Environmental Science, University of Pittsburg, Pittsburgh, PA, 15260, USA. [5]NASA Langley Research Center, Hampton, VA, 23666, USA. [6]Analytical Mechanics Associates (AMA), Hampton, VA 23666. [7]Science Systems and Applications, Inc., Lanham, MD, USA. [8]The Department of Earth, Ocean, and Atmospheric Science, Florida State University, Tallahassee, FL, 32304, USA. [9]Department of Biological Sciences, Florida International University, Miami, FL, 33199, USA. [10]Department of Coastal Studies, East Carolina University, Greenville, NC, 27858, USA. [11]Yale School of the Environment, Yale University, New Haven, CT, 06511, USA. [12]Department of Biological Sciences, University of Alabama, Tuscaloosa, AL 35487, USA. [13] Department of Earth and Environment, Florida International University, Miami, FL, 33199, USA. [14] Biospheric Sciences Laboratory, NASA Goddard Space Flight Center, Greenbelt, MD 20771, USA.

Corresponding author: Erin R. Delaria (erin.r.delaria@nasa.gov)

† Current address: Atmospheric Science Branch, NASA Ames Research Center, Moffett Field, CA, 94035, USA

Key Points:

- Airborne eddy covariance measurements reveal heterogeneity in CH_4 and CO_2 fluxes across southern Florida.
- Variability in carbon fluxes were primarily driven by vegetation types, season, ecosystem productivity, and soil inundation.
- Southern Florida served as a net carbon sink during all flight periods, with CH_4 emissions offsetting CO_2 deposition by 11–91%.

Abstract

Coastal wetlands play a significant role in the storage of 'blue carbon', indicating their importance in the carbon biogeochemistry in the coastal zone and in global climate change mitigation strategies. We present airborne eddy-covariance observations of CO_2 and CH_4 fluxes collected in southern Florida as part of the NASA BlueFlux mission during April 2022, October 2022, February 2023, and April 2023. The flux data generated from this mission consists of over 100 flight hours and more than 6000 km of horizontal distance over coastal saline and freshwater wetlands. We find that the spatial and temporal heterogeneity in CO_2 and CH_4 exchange is primarily influenced by season, vegetation type, ecosystem productivity, and soil inundation. The largest CO_2 uptake fluxes of more than 20 µmol m^{-2} s^{-1} were observed over mangroves during all deployments and over swamp forests during flights in April. The greatest CH_4 effluxes of more than 250 nmol m^{-2} s^{-1} were measured at the end of the wet season in October 2022 over freshwater marshes and swamp shrublands. Although the combined Everglades National Park and Big Cypress National Preserve region was a net sink for carbon, CH_4 emissions reduced the ecosystem carbon uptake capacity (net CO_2 exchange rates) by 11–91%. Average total net carbon exchange rates during the flight periods were -4 to -0.2 g CO_2-eq m^{-2} d^{-1}. Our results highlight the importance of preserving mangrove forests and point to potential avenues of further research for greenhouse gas mitigation strategies.

Plain Language Summary

Coastal wetlands play a crucial role in trapping and storing carbon, aiding in climate change adaptation and mitigation efforts. Carbon dioxide (CO_2) uptake and methane (CH_4) emissions were measured from an aircraft over wetlands of southern Florida during different times of the year. Season, vegetation, ecosystem productivity, and water depth were found to have a large influence on carbon exchange. Mangroves with the largest canopy heights showed the highest CO_2 uptake, while CH_4 emissions peaked during the wet season over freshwater marshes where surface water depths were greatest. CH_4 emissions diminished the overall carbon uptake capacity of southern Florida. Results emphasize the importance of preserving coastal wetland ecosystems and suggest potential directions for further research aimed at mitigating greenhouse gas emissions.

1 Introduction

Vegetated ecosystems mitigate the impact of anthropogenic CO_2 emissions by serving as natural carbon stores (e.g., Barbier et al., 2011; Donato et al., 2011; Murdiyarso et al., 2015; Duarte 2017). The terrestrial biosphere is estimated to remove 10–40% of the CO_2 emitted from fossil fuels, and coastal aquatic vegetation removes a further 3–25% (Barbier et al., 2011; Donato et al., 2011; Murdiyarso et al., 2015; Duarte 2017; Friedlingstein et al., 2023). Coastal vegetated ecosystems have been of recent interest for “blue” carbon mitigation strategies because of their efficiency for short-term carbon storage in vegetation biomass (above- and belowground) and long-term carbon storage in soils and sediments (e.g., McLeod et al., 2011; Barbier et al., 2011; Donato et al., 2011; Murdiyarso et al., 2015; Macreadie et al., 2021; Poulter et al., 2023). “Blue” carbon refers to the carbon that is captured by oceans and coastal ecosystems. Although coastal vegetated ecosystems (i.e., mangroves, salt marshes, seagrasses) cover an area equivalent to ~2% of terrestrial forest area, their carbon burial rates are 50 times faster per unit area, making the net contributions of coastal wetlands to carbon sequestration comparable to that of terrestrial forests (McLeod et al., 2011; Duarte et al., 2013). Yet these ecosystems are under continued threat due to hurricanes, land development, and sea level rise, which contribute to a global net loss of mangroves and salt marshes at a rate of 0.13–2% annually (McLeod et al., 2011; Goldberg et al., 2020; Campbell et al., 2022; Murray et al., 2022).

Understanding the climate change mitigation potential of these ecosystems requires accurate accounting of their carbon balance. Only a fraction of the CO_2 taken up by coastal vegetation is sequestered in sediments via long-term carbon burial. Much of this carbon is stored in shorter-term above- and belowground biomass, re-emitted to the atmosphere through soil respiration, or transported to the ocean as particulate organic carbon (POC), dissolved organic carbon (DOC), and dissolved inorganic carbon (DIC) (Rosentreter 2018b; Sanderman et al., 2018; Simard et al., 2019; Adame et al., 2021). In addition, anoxic soil conditions and methanogenic archaea in coastal vegetated ecosystems produce CH_4 (e.g. Bartlett et al., 1987; Rosentreter 2018c; Al-Haj and Fulweiler, 2020). Methane emissions have the potential to significantly offset the climate mitigation potential of coastal wetlands, as the global warming potential (GWP) of methane is 81.2 and 27.9 times greater than that of CO_2 on a 20- and 100-year scale, respectively (Forster et al., 2021). Estimates of global CH_4 emissions from coastal wetlands are poorly constrained, with uncertainties stemming from large regional differences, lack of direct measurements, and anthropogenic impacts on wetland disturbance and hydrology (Harrison et al., 2017; Kroeger et al., 2017; Saunois et al., 2020; Rosentreter et al., 2021).

Several methods exist for quantifying carbon exchange at landscape to global scales, each with their own benefits and limitations. Concentration measurements from aircraft, ground sites, and satellites can be coupled with inverse models to provide a "top-down" inference of atmosphere-biosphere CO_2 and CH_4 exchange (e.g. Wang et al., 2018; Saunois et al., 2020; Ma et al., 2021; Schiferl et al., 2022; Gaubert et al., 2023). However, these top-down approaches suffer from considerable uncertainties related to atmospheric transport and heavily rely on prior assumptions for source attribution. Satellite-based top-down approaches allow for the assessment of changes in CO_2 and CH_4 fluxes over multiple years with global coverage, which is particularly important in areas where direct ground-based and airborne measurements are limited (e.g., Campbell et al., 2020). Satellite approaches are, however, further limited by additional uncertainties related to satellite retrievals. Bottom-up inferences of carbon atmosphere-biosphere exchange in wetlands utilize biophysical process models, inventories of biomass, and remotely sensed surface properties to indirectly calculate fluxes (Hayes et al., 2018; Saunois et al., 2020; Ma et al., 2021; Friedlingstein et al., 2022; Zhang et al., 2023). These models, however, rely on complicated parameterizations and assumptions of biological activity across a complex diversity of ecosystems and environmental conditions. This leads to large uncertainties, disagreements between different modeling approaches, and inconsistencies between top-down and bottom-up methods (Melton et al., 2013; Pandey et al., 2021; Saunois et al., 2020; Ma et al., 2021).

Alternatively, atmosphere-biosphere fluxes can also be measured directly on a variety of scales and can provide a more discerning understanding of wetland fluxes in space and time. Ground-based chamber measurements are important for quantifying process-level drivers of carbon exchange from soils, leaves, roots, and stems (e.g. Nahlik and Mitsch 2011; Marín-Muñiz et al., 2015; Troxler et al., 2015; Rosentreter et al., 2018a). Chamber water-atmosphere CH_4 and CO_2 fluxes coupled to measurements of water properties have identified factors controlling the cycling of carbon in mangrove-dominated Australian estuaries and tidal freshwater marshes in Veracruz, Mexico (Marín-Muñiz et al., 2015; Rosentreter et al., 20218a). These types of studies are extremely useful for linking carbon fluxes to underlying processes, but measurements are typically only conducted for a short period of time at a limited number of sites, making upscaling these findings difficult and sensitive to statistical assumptions.

Eddy covariance flux towers provide localized representations of net ecosystem exchange (NEE) fluxes over longer periods (e.g., Barr et al., 2010; Beringer et al., 2013; Malone et al., 2015; Shoemaker et al., 2015; Alvarado-Barrientos 2020; Zhu et al., 2021). Such EC towers have been used to quantify the seasonality of net ecosystem CO_2 exchange in mangrove forests in the Florida Everglades (Barr et al., 2010; Barr et al., 2012), the Yucatan Peninsula (Alvarado-Barrientos 2020), and southeastern China (Zhu et al., 2021). But the degree to which measurements at one flux tower are representative of other sites varies, even within the same region, as environmental conditions (e.g. soil properties, inundation, leaf area, tidal influence, etc.) can vary from region to region and from site to site.

Airborne eddy covariance (EC) offers a viable approach to measure fluxes over larger areas, though with a more limited temporal resolution (e.g. Crawford et al., 1996; Sellers et al., 1997; Zulueta et al., 2013; Wolfe et al., 2015; Desjardins et al., 1982; Wolfe et al., 2018; Hannun et al., 2020). This technique has the advantage of elucidating heterogenous fluxes over a large region (15-100 km) at a relatively fine spatial scale (~1km). One recent application of the technique in a tropical Zambian wetland highlighted large discrepancies between land surface models and observations (Shaw et al., 2022). Zulueta et al. (2013) also utilized airborne EC to derive heterogenous CO_2 fluxes over distinct ocean, mangrove, and desert ecosystems in Baja California Sur, Mexico. This latter study also utilized tower flux measurements and vegetation indices to assess the representativeness of towers and provide a simple model for scaling up to regional CO_2 fluxes. However, these studies represent two of only very few that have used airborne EC to measure greenhouse gas exchange in subtropical to tropical wetlands.

Here we analyze extensive airborne CO_2 and CH_4 flux measurements acquired over southern Florida during the NASA BlueFlux mission. Combining flux measurements and flux footprint analysis with detailed information of land surface properties, we explore the patterns in flux variability across this diverse landscape. We also utilize long-term ground-based flux datasets to provide a valuable point of comparison and a means of upscaling to estimate the net regional carbon balance. Although the definition of “blue” carbon typically only includes tidal saltwater wetlands, we also investigate carbon exchange in the freshwater wetlands within the greater Everglades coastal watershed system. These regions are also extremely influential in the carbon cycle of this coastal zone. The primary objectives of this study are to 1) elucidate the heterogeneity of atmosphere-biosphere carbon fluxes in southern Florida, 2) identify the underlying sources of this variability, and 3) provide an estimate of the net carbon balance during the sampling periods from an atmospheric perspective. In addressing each of these objectives, we identify potential avenues for applying our unique data set to addressing “blue” carbon greenhouse mitigation strategies.

2 Materials and Methods

2.1 BlueFlux Field Campaign

BlueFlux is a NASA-sponsored effort to understand the dynamics of carbon exchange in coastal wetlands and develop long-term gridded flux estimates for science and policy applications. The BlueFlux field campaign was developed to provide comprehensive measurements of ecosystem carbon fluxes in southern Florida, with a special emphasis on mangroves. BlueFlux observations bridge multiple scales of biosphere-atmosphere exchange, including chamber measurements of soil and vegetation fluxes, ecosystem-scale fluxes from existing EC tower sites, airborne EC measurements across the south Florida region, and lateral aquatic carbon fluxes (Poulter et al., 2023). Primary study regions include Everglades National Park (ENP) and Big Cypress National Preserve (BCNP) (Fig. 1). The focus of this study is the airborne EC component of the project.

Southern Florida is characterized by a subtropical to tropical climate. The wet season occurs from May through October, during which conditions are hot (>30ºC) and humid (>80% relative humidity) with frequent convective thunderstorms. The average annual rainfall is typically 1000–1700 mm, with 70% of precipitation occurring during the wet season (Florida Climate Center https://climatecenter.fsu.edu/products-services/data/statewide-averages/precipitation). The dry season (November to April) is typically warm (13–22 ºC) and dryer, with very rare winter frosts projected to decrease over time (Ross et al., 2009). Flights were performed during April 2022, October 2022, February 2023, and April 2023. April months are typically in the tail-end of the dry season and beginning of the wet season, while October is considered the tail-end of the wet season. Temperatures during study months were roughly average for the area and season, and ENP and BCNP experienced an average amount of rainfall during April 2022 and October 2022. However, Hurricane Ian made landfall north of the study region on September 28, 2022. There were higher observed water levels in the weeks following the hurricane at EC tower sites (EDEN, https:sofia.usgs.gov/eden). Conversely, February 2023 and April 2023 experienced below average rainfall that was 26% and 73%, respectively, of normal levels (South Florida Water Management District https://www.sfwmd.gov/weather-radar/rainfall-historical/year-to-date). Atlantic basin hurricanes frequently pass over Southern Florida between August and November. Such hurricanes have resulted in significant alteration to the coastal wetlands of Southern Florida over the past 32 years (Taillie et al., 2020). The terrain is mostly flat, with some small hills (up to 6 m above mean sea level) in the northwest portion of BCNP.

2.2 Airborne flux measurements

2.2.1 Flight strategy

Airborne operations utilized a Beechcraft King Air A90 owned and operated by Dynamic Aviation. Deployments entailed four 2-week intensives, each consisting of 6–8 flights with durations of 2–4 hours each (~25 flight hours per deployment). A typical flight consisted of straight and level legs at an altitude of 90 m above mean sea level and a ground speed of 65–80 m s^{-1}, along with occasional overlapping legs at higher altitudes (up to 300 m) to constrain flux divergence. Vertical profiles were performed periodically (up to 3 km) to ascertain boundary layer depth. Flux legs were typically oriented across the mean horizontal wind flow, spanned lengths of 20–100 km, and concentrated on mangrove forests and regions of recent mangrove dieback ('ghost' forests) (Fig. 1) that resulted from impacts of Hurricane Irma (September 2017) (Lagomasino et al., 2021). Other considerations for flight design included overflight of existing ground sites and avoidance of nesting bird colonies and Seminole and Miccosukee tribal lands. In total, flux transects during all deployment periods comprise more than 6000 km of linear distance.

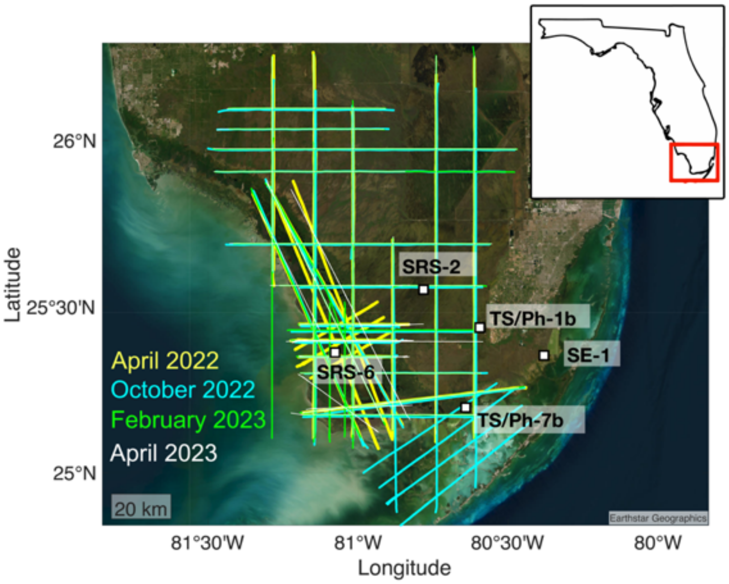

Figure 1: Flux transects from all flights between April 2022 and April 2023. Flux legs from April 2022, October 2022, February 2023, and April 2023 are shown in yellow, cyan, green, and white, respectively. The locations of five ground sites with eddy covariance towers are indicated with square markers.

2.2.2 Instrument Payload

The BlueFlux study utilized an upgraded version of the NASA Carbon Airborne Flux Experiment (CARAFE) platform, originally described by Wolfe et al. (2018). Ambient air was sampled from a common inlet (1.3 cm stainless steel with fluoropel coating) located under right wing. The sample tube was fluorinated ethylene propylene (FEP) with an inner diameter of 0.65 cm and a length of about 8 m. Gas measurements utilized two commercial Picarro closed-path analyzers. A model g2311f (hereafter, PFlux) provided continuous measurements of CH_4, CO_2 and H_2O at 10 Hz, while a model g2401m (hereafter PConc) provided measurements of CH_4, CO_2, H_2O, and CO at 0.5 Hz. Agilent IDP3 scroll pumps maintained gas flows of ~5.5 slm and ~1 slm, respectively. The greater pressure stability of the PConc (which is designed for flight) provides an accuracy standard, while the PFlux provided the fast measurements required for eddy covariance. Supplement Section S1 describes comparisons and corrections for the two instruments. The PConc was calibrated in the lab before and after each mission (see Sect 2.2.3).

An Aventech Aircraft-Integrated Meteorological Measurement System (AIMMS-20) provided 20 Hz measurements of aircraft position and attitude, air temperature and pressure, and 3-D wind velocities. The probe was mounted under the left wing and calibrated via the manufacturer-provided protocol at the start of each deployment.

2.2.3 Flux calculations

Data from the AIMMS-20 probe (20 Hz vertical wind speed, w, and potential temperature, Θ), and the 10-Hz measurement of H_2O, CO_2, and CH_4 were time aligned to a common 10-Hz time base and combined to determine fluxes of CH_4, CO_2, latent heat (LE) and sensible heat (H) using airborne eddy covariance with the continuous wavelet transform (CWT) method (Torrence and Compo, 1998; Wolfe et al., 2018). Flux legs were selected as flight segments greater than 15 km in linear distance with an aircraft roll not exceeding 5^o and altitude variation within ± 10 m. Scalar time series were detrended by subtracting a 40-second (~4 km) moving average and time-shifted by 0 to 3 s based on lag correlation to the vertical wind (Fig. S4). This detrending length was selected to remove non-turbulent variability and maintain the largest eddies contributing to the flux (Moncrieff et al., 2006).

Following this pre-processing of the data, fluxes were calculated using CWT (Section S2). Flux data for analysis is filtered by the cone of influence (COI), i.e., the spectral region where additional errors and uncertainties may be present due to edge effects (Torrance and Compo, 1998). Data are excluded where the fraction of the cospectral power that resides within the COI is greater than 0.5. Fluxes are further filtered to exclude measurements where the friction velocity (u^*)—as determined from momentum fluxes at aircraft height (Section 2.4.3)—is less than 0.2 m s^{-1} over land, or less than 0.1 m s^{-1} over water. This criterion was selected to exclude periods with insufficient vertical mixing (e.g. Hogstrom 1988; Barr et al., 2010; Hayek et al., 2018). The selected $u*$ filtering limits are in accordance with EC towers (Barr et al., 2010) and were verified for flight data with the method of Hayek et al., 2018.

2.2.4 Uncertainties

Systematic error contributions to flux uncertainties include those due to under-sampling of low frequencies (SE_{turb}), the instrument response time which can limit detection of high-frequency signals (SE_{RT}), and instrument accuracy (SE_{acc}). SE_{RT} and SE_{turb} were calculated according to Wolfe et al., 2018. The e-folding response time used to calculate SE_{RT} was determined through laboratory tests to be 90 ± 10 ms for the PFlux instrument—which translates to an effective cutoff frequency of 3.8 Hz. SE_{acc} for each scalar is based on measurement accuracy. Accuracy for CH_4 and CO_2 measurements are 0.05%, and 0.2%, respectively, determined through laboratory calibration with WMO-grade calibration NOAA cylinders (IDs CC746186 and CA03516). The PFlux stated H_2O accuracy is 0.8%. The AIMMS-20 probe has a stated accuracy of 10% for vertical wind speed.

Random errors in fluxes include contributions from uncorrelated instrument noise and turbulent variability. Methods have been developed for traditional ensemble-averaged EC to represent the individual contributions of these two sources of uncertainty, as well as to empirically calculate the total random error based on the cross- and auto- covariance of scalar *s* and *w* at different time lags (e.g. Leschow et al., 1994, Finkelstein and Simms, 2001). It is not immediately obvious how these approaches are best applied to time-resolved CWT analysis. Here we propose a new method for quantifying random flux errors (RE) for CWT based upon Langford et al. (2015). In this approach, the root mean squared deviation from zero of the cross-covariance between *s* and *w* is used to represent the random flux error (RE):

$$RE = \sqrt{N}\sqrt{\left(0.5\left(\left(\sigma_{w's'[-\Gamma]}\right)^2 + \left(\overline{f_{w's[-\Gamma]}}\right)^2 + \left(\sigma_{f_{w's'[+\Gamma]}}\right)^2 + \left(\overline{f_{w's'[+\Gamma]}}^2\right)\right)\right)^2} \quad (1)$$

Here N is the number of data points per second, $\sigma_{w's'}$ is the standard deviation of the covariance ($f_{w's'}$) and $\overline{f_{w's'}}$ is the average cross-covariance over a time lag range of $-\Gamma$ or $+\Gamma$. Primes denote deviations from the mean of *w* and *s*. We define Γ over a time lag range from one to 100 data points. Here, 100 was chosen as the maximum lag considered for Γ to be representative of the integral time scale. This representation considers the variability in the cross-covariance of *s* and *w*, as well as the offset from zero related to non-turbulent trends in the data.

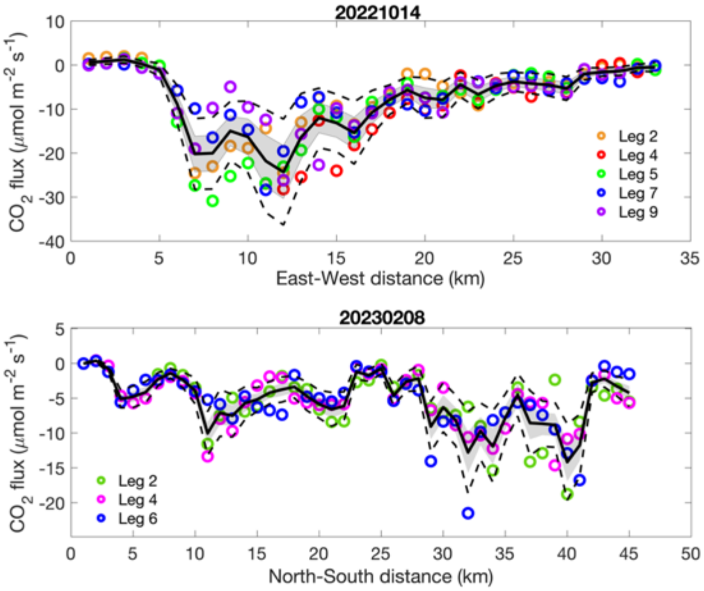

Figure 2: CO_2 fluxes for repeated legs over the same flight path on October, 14, 2022 (top) and February 8, 2023 (bottom). Colored markers represent 1 km average fluxes for the different legs. Solid black lines, shading, and dotted lines represent the mean flux, 1σ random error, and 2σ random error, respectively.

Random flux errors vary along flux legs due to variations in turbulence and tend to be larger in magnitude for larger magnitude fluxes. For 1-Hz-averaged flux measurements, the median limit of detection (LOD), defined as twice the median random flux error, is 2.8 µmol m^{-2} s^{-1} and 18.3 nmol m^{-2} s^{-1} for CO_2 and CH_4 fluxes, respectively. Average fluxes at 1 km resolution have a median LOD of 0.9 µmol m^{-2} s^{-1} and 5.8 nmol m^{-2} s^{-1} for CO_2 and CH_4 fluxes, respectively. This error is approximately a factor of three lower than that derived using the approach of Wolfe et al. (2018), which was calculated from the sum (rather than the standard deviation and mean) of the cross covariance between *s* and *w* in analogy to Finkelstein and Sims (2001). Random fluxes were also estimated experimentally over a leg on April 19, 2022, by overflowing the inlet with calibration gas. The standard deviation of the 10-Hz CO_2 "flux" was 0.7 µmol m^{-2} s^{-1} (mean -0.0045 µmol m^{-2} s^{-1}), providing an estimation of combined instrument noise and turbulence random errors over this leg. We found the approach of Wolfe et al. (2018) to result in an unreasonably large random flux error over the same flight track of 9.0 µmol m^{-2} s^{-1}, compared with our new parameterization (3.3 µmol m^{-2} s^{-1}) (Figure S11).

During each flight we performed repeat flux legs over the same ground track above a mangrove forest to provide an additional test of the variability in flux measurements due to random error. Figure 2 shows 1km-averaged CO_2 fluxes from repeat legs during two different flight patterns flown in October 2022 and February 2023. Leg-to-leg variability typically falls within that expected based on random errors estimated via Eqn. (1), providing further validation of the calculated random flux errors.

We include an additional uncertainty estimate from the vertical divergence of fluxes (see Supplementary Information Section S5). During each flight we performed vertically stacked legs to estimate the change in flux with altitude and allow for extrapolation of fluxes to the surface. In most cases the differences in calculated surface fluxes and fluxes measured at the aircraft altitude (< 100 m) were not statistically significant ($\alpha = 0.05$, two-sided t-test). This is not surprising, as the aircraft altitude was typically in the lowest 10 % of the boundary layer. We therefore assume that the surface fluxes are equal to the aircraft altitude fluxes and include the difference between the extrapolated surface flux and flux measured at the aircraft altitude as an additional systematic error. We do not correct the reported fluxes for the calculated surface flux divergence because this correction uncertainty is typically much larger in magnitude than the correction itself, which would thus introduce even greater uncertainty. The magnitudes of all contributing flux errors are shown in Figure S12. The largest sources of systematic uncertainty are divergence effects (IQR 3-30%) and SE_{acc} (10%). The effect of RE is small when averaged over a flux leg (IQR 1–5% uncertainty), but large for 1-Hz fluxes (IQR 30–60 % uncertainty)

2.3 Flux towers

Several flux towers located in the Everglades regions of southern Florida measure half-hourly fluxes of CO_2, CH_4, sensible heat (H), and latent energy (LE) using the eddy covariance method. These towers are part of the Florida Coastal Everglades Long-Term Ecological Research (FCE LTER) and the AmeriFlux tower networks. Towers are located along the Shark River Slough (SRS) and the Taylor Slough/Panhandle (TS/Ph) (Fig. 1) hydrologic gradients (Barr et al., 2010; Malone et al., 2015) and are representative of freshwater marsh (SRS-2), freshwater marsh prairies (TS/Ph-1), mangrove forests (SRS-6) and mangrove scrub (TS/Ph-7). These EC towers measure vertical wind speed and virtual temperature with 3D sonic anemometers (SRS-6: model RS-50, Gill Co., Lymington, England; SRS-2, TS/Ph-7, and TS/Ph-

1: CSAT 3B, Campbell Scientific Inc., Logan, Utah). CO_2/H_2O (LI-7500) and CH_4 (LI-7700) are measured at 20 Hz with open path infrared gas analyzers (LI-COR, Inc., Lincoln, Nebraska).

2.4 Flux decomposition by land classification

Southern Florida is a heterogenous landscape with a wide range of vegetation types. Vegetation phenology, quantity, and productivity modulate CO_2 uptake. Other features like salinity, water levels, surface water extent, tides, inundation period, and soil moisture can lead to changes in CH_4 emission fluxes and biological CO_2 respiration. We consider several geographical data sets to identify some of the causes of the observed variability in GHG fluxes across the flight domain.

2.4.1 Vegetation coverage

Land cover and vegetation information for ENP and BCNP was obtained from Ruiz et al. (2019, 2021) and Whelan et al. (2020). Land classifications based on these data sets included 16 different classes (Fig. 3) at 50 m spatial resolution. Dominant land classifications sampled during BlueFlux over ENP and BCNP were freshwater marsh (21%), mangrove forest (17%), mangrove scrub (10%), mangrove shrubland (6.6%), salt marsh (2.2%), swamp forest (6.9%), swamp scrub (7.5%), swamp shrubland (5.7%), and upland forest (3.5%). The “Ghost Forest” land class was added to identify where mangrove forests experienced extensive die-offs by drowning following Hurricane Irma in 2017 (Lagomasino et al., 2021). Ghost forests constituted 2.2% of all land classes sampled, and 13% of the mangrove forest sampled. Dominant vegetation species found in each class are listed in Supplementary Information Section S3. Some flight tracks are outside of the ENP and BCNP boundaries and are therefore not included in the vegetation analysis.

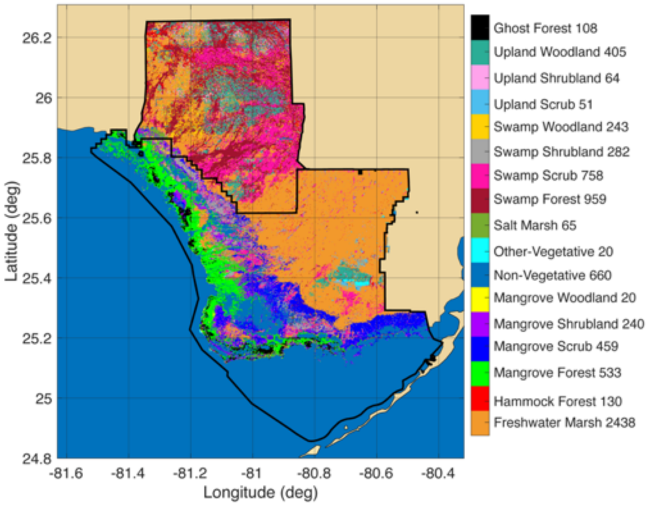

Figure 3: Map of vegetation coverage for the Everglades National Park (ENP) and Big Cypress National Preserve (BCNP) regions. Figure adapted from Ruiz et al. (2019, 2021) and Whelan et al., (2020). The ghost forest area was adapted from Lagomasino et al. (2021). Numbers following the vegetation types in the figure legend denote the area of each region in

units of km^2. Black solid lines denote the boundaries of ENP in the south and BCNP in the north.

2.4.2 Other surface characteristics

Remotely sensed satellite products of enhanced vegetation index (EVI), normalized difference vegetation index (NDVI), leaf area index (LAI), the fraction of photosynthetically active radiation (400-700 nm) absorbed by green vegetation (FPAR), and soil moisture were obtained over South Florida as an average for each flight month. The vegetation indices were obtained from the Moderate Resolution Imaging Spectroradiometer (MODIS) on the Terra satellite at a resolution of 250 m (Didan et al., 2015). LAI and FPAR were acquired from the combined MODIS Terra + Aqua land data products at 500 m resolution (Myneni et al., 2015). The Soil Moisture Active Passive mission (SMAP) provided a remotely sensed soil moisture product at 9 km resolution (O'Neil et al., 2023). Above ground biomass density (AGBM) and canopy heights for the study region were estimated from the Global Ecosystem Dynamics Investigation (GEDI) Lidar 2021 data products at 1 km resolution (Dubayah et al., 2021, 2023).

The Everglades Depth Estimation Network (EDEN, https:sofia.usgs.gov/eden) provides a long-term daily estimate of surface water-level. This data set consists of surface water depth estimates at 400 m resolution obtained from a model that interpolates measurements from a dense network of water gauges through the Everglades and water management areas of South Florida (Haider et al., 2020).

2.4.3 Footprint analysis

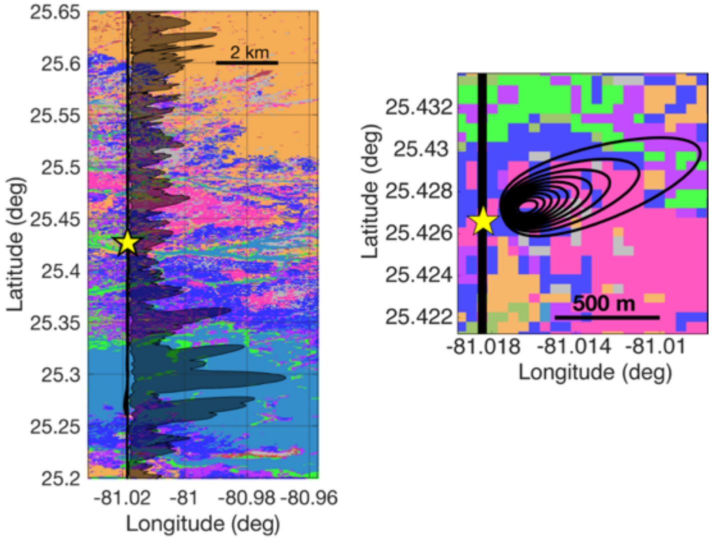

Figure 4: (**Left**) a single flux transect at 90 m altitude from the flight on April 19, 2023 superimposed on the map of vegetation cover. The shaded area shows the cumulative footprint containing the area contributing to 90% of the flux signal. (**Right**) A single footprint at the measurement location marked with the star. Contours depict the weighted contributions to the observed flux from 10% to 90% in 10% increments. Background colors denote land classification (Fig. 2).

Along each flux segment below 100 m altitude we computed a 2D flux footprint that expresses the relative contribution of each upwind surface element to the observed flux. This footprint analysis is detailed in Hannun et al. (2020). Briefly, to compute the flux footprint we used the parameterization of Kljun et al. (2015) based on a Lagrangian stochastic particle dispersion model (Kljun et al., 2002). Inputs to the 2D footprint calculation include the measurement height, mean horizontal wind speed (U), planetary boundary layer (PBL) height, the Obukhov length (L_{OB}), standard deviation of the lateral velocity fluctuations (σ_v), and the friction velocity (u^*). For these calculations we used the PBL height obtained from the High-Resolution Rapid Refresh (HRRR) 3 km product interpolated along our flight track. HRRR PBL height was validated against single-point determinations of actual PBL height based on observations of trace gas vertical profiles during each flight. We calculated u^* from the momentum fluxes of the horizontal winds u and v (also determined with the CWT) and validated u^* with measurements from the Everglades network of EC towers (Fig. S13 and S14). The flux footprint was then rotated into the mean wind direction and translated to geographical coordinates. Example flux footprints along a flight track are shown in Figure 4. For segments below 100 m altitude, 90 % of the flux signal is contained within a region 1–2 km up wind of the measurement location over land. Footprints are typically larger over water, with 90% of the flux signal contained within 5 km of the measurement point.

2.4.4 Flux disaggregation

The observed flux contains contributions from the fluxes of different land classes contained within the flux footprint. To derive the mean flux for each vegetation type over a set of flux observations (e.g., flux leg, single flight, or period of deployment), we used the method described in Hannun et al. (2020). This method utilizes the Disaggregation combining Footprint analysis and Multivariate Regression (DFMR) technique of Hutjes et al. (2010). Here the observed flux is treated as a linear combination of component fluxes from each land class within the footprint, such that:

$$F_{obs} = \sum_{k=1}^{n} C_k F_k \qquad (6)$$

C_k is the fractional contribution of the k^th^ land class to the flux footprint, and F_k is the average flux from the corresponding land class over the observation period. C_k for each 1 Hz flux observation was determined by overlaying the footprint function onto a gridded map of land cover (Fig 3, Fig 4) and weighting by the contribution of each grid cell to the observed flux (areas closer to the measurement point contribute more heavily to the measurement). F_k was calculated via multilinear regression of F_{obs} versus C_k for each land class that constituted more than 25% of the flux footprint over more than 10 linear km of cumulative (but not necessarily consecutive) observations. This criterion was selected to ensure sufficient sampling of each land class during the observation period. The regions that met this criterion were mangrove forests, mangrove scrub, mangrove shrubland, ghost forest, salt marsh, freshwater marsh, swamp shrub, swamp scrub, swamp forest, and upland forest.

Uncertainty in mean fluxes for each land class was calculated as the statistical uncertainty in the regression. Random and systematic errors, as well as the calculated divergence correction (summed in quadrature to yield the total uncertainty) for each flux observation were also propagated through the regression analysis. We do not include uncertainties in the land surface data or the footprint analysis, as we expect these to be comparatively small (Hannun et al., 2020).

Disaggregation of fluxes from additional categorical land data were computed using the same method as for vegetation data. Continuous numerical land cover data, such as NDVI, do not require multivariate regression to disaggregate fluxes. After superimposing the footprint function onto the geographical data set, the footprint weighted average of the land cover data can simply be calculated at each 1-Hz observation in the same manner as for fractional land class contributions (e.g., C_k).

3 Results and Discussion

3.1 Heterogenous CWT-derived Fluxes

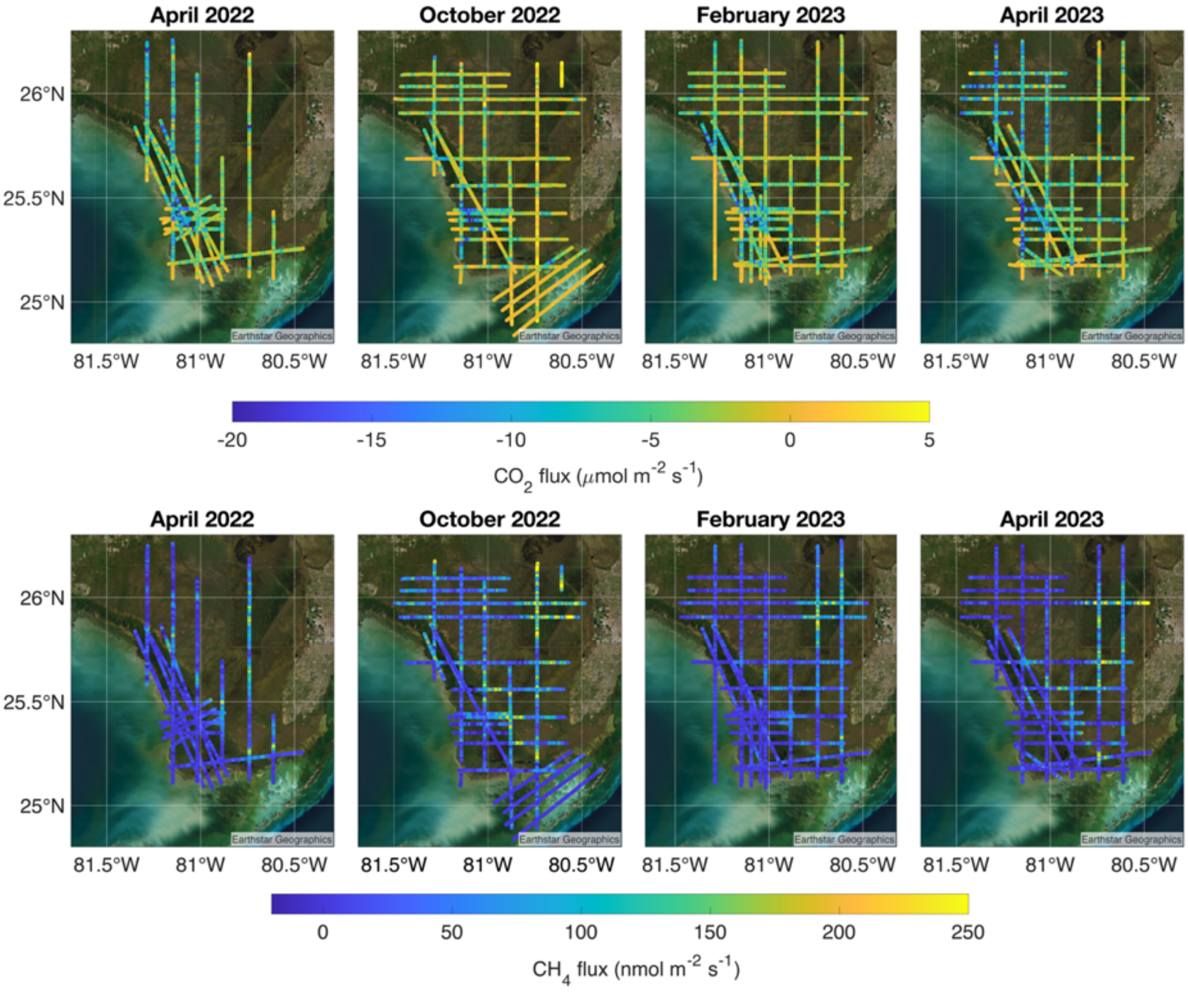

Figure 5: Spatial distribution of (top) CO_2 and (bottom) CH_4 1 km averaged fluxes over flight legs below 100 m altitude for all seasons. Here negative fluxes denote uptake and positive fluxes represent emission. Flux rates are color coded to scale below maps. Larger CO_2 uptake fluxes appear as darker colors, while larger CH_4 emissions appear as brighter colors

The airborne CWT derived fluxes measured below 100 m flight altitude are shown in Figure 5. Negative and positive fluxes represent uptake and emission by the surface, respectively. These fluxes provide a measurement of the net ecosystem exchange of CO_2 and CH_4, as the aircraft samples the net canopy exchange (photosynthetic uptake, respiration, and storage) of carbon. Downward (i.e., uptake) CO_2 fluxes are largest (less than -15 µmol m^{-2} s^{-1})

during all flight periods over mangrove forests in the southwest portion of the flight domain, near 25°30’ N and 81° W. During both April deployments, high rates of CO_2 uptake were also observed in the northwest quadrant over the swamp and upland forests of BCNP.

Methane fluxes also demonstrate significant spatial heterogeneity during all deployment periods. The largest methane fluxes (greater than 200 nmol m^{-2} s^{-1}) occur in the northeast portion of the flight domain over freshwater marshes. High CH_4 emissions also appear in a band just inland of the west coast in the transition region between mangroves and marshlands (Fig 3, Fig 5).

3.2 Drivers of CO_2 uptake and CH_4 emission

3.2.1 Vegetation class

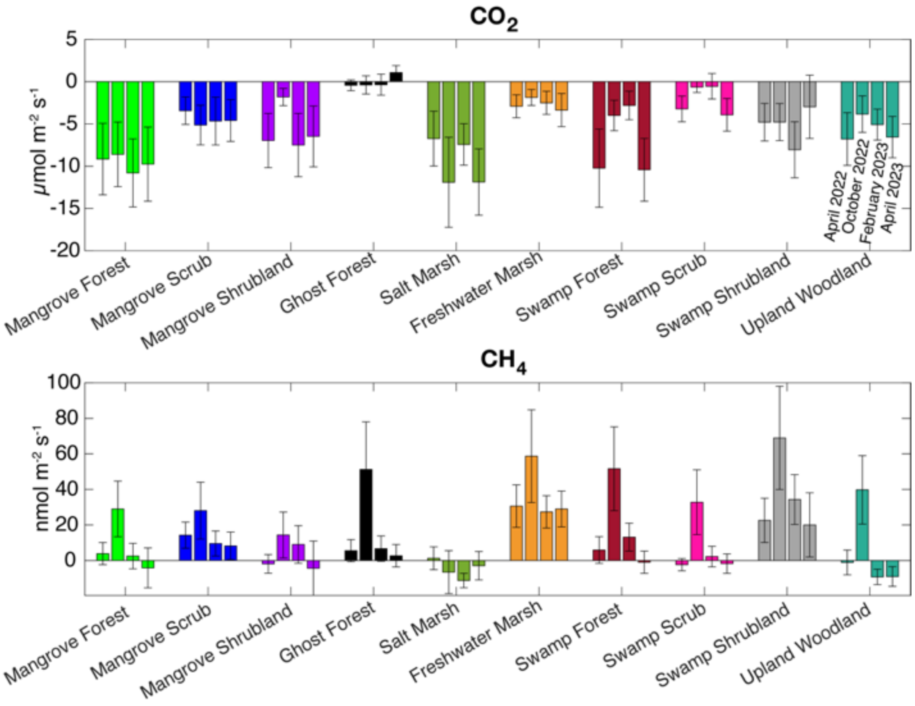

Figure 6: CO_2 and CH_4 fluxes disaggregated by land class for all flights during April 2022, October 2022, February 2023, and April 2023. Fluxes are grouped by vegetation coverage. Error bars represent ±1σ uncertainty in the component flux, which includes systematic, random, and divergence flux uncertainties propagated through the regression analysis, in addition to the regression residuals, which also reflect the variability in carbon fluxes for each vegetation regime.

Figure 6 shows that CO_2 and CH_4 fluxes clearly and consistently vary according to the underlying vegetation type. In some cases, there is also an apparent seasonality in the fluxes. Disaggregated fluxes demonstrate that the largest fluxes of CO_2 uptake were observed for mangrove forests, salt marshes and swamp forests. The greatest CH_4 emissions were consistently measured over freshwater marshes and swamp shrublands. Below we discuss in detail the patterns in observed carbon exchange for mangrove, salt marsh, freshwater wetlands, and upland ecosystems.

Mangroves

Mangrove forest CO_2 fluxes did not exhibit much variation over the different sampling months, with the largest average uptake rate of -11 ± 4 μmol m^{-2} s^{-1} observed during February 2023. These fluxes are consistent with the range of -5 to -18 μmol m^{-2} s^{-1} uptake observed in the Yucatan during 2017–2018 from an eddy-flux tower (Alvarado-Barrientos et al., 2021). Large peak daily fluxes of -13 to -20 μmol m^{-2} s^{-1} and -17.1 to -19.9 μmol m^{-2} s^{-1} have been observed in coastal southeastern China (Zhu et al., 2021) and near Hong Kong (Liu and Lai 2019), respectively. Weak seasonality of CO_2 fluxes was also observed in both other regions. We regularly observed fluxes of -17 to -22 μmol m^{-2} s^{-1} near the SRS-6 tower site in southwestern ENP, where previous studies have reported the highest mangrove above-ground biomass and productivity (Castañeda-Moya et al., 2013; Danielson et al., 2017; Rivera-Monroy et al., 2019) (Fig. 5, Fig S17, Fig S18). Barr et al. (2010) reported peak uptake values between -15 and -25 μmol m^{-2} s^{-1} at the SRS-6 tower site prior to Hurricane Wilma in 2005, suggesting the strong carbon sink capacity of these riverine mangroves. Our smaller average midday CO_2 fluxes compared with other regions of mangroves may in part be due to lasting effects of past hurricanes. Hurricane Andrew in 1992 had devastating impacts on mangrove forests (Smith et al., 2005). Although trees recovered, canopy heights are still lower in some areas than pre-Andrew levels. High winds and large storm surges from Hurricane Irma in 2017 also created ghost forests and caused additional canopy height loss (Lagomasino et al., 2021).

Average mangrove shrub CO_2 fluxes were very similar to the -8.11 μmol m^{-2} s^{-1} fluxes measured for mangroves of similar heights and speciation in Baja California Sur, Mexico (Zulueta et al., 2013). Lesser average uptake of -3 to -5 μmol m^{-2} s^{-1} was measured for mangrove scrub systems, which have a lower average canopy height (< 2 m) compared to mangrove shrublands (2-5 m) and forests (>5 m). The mangrove shrublands exhibit greatly reduced CO_2 uptake during October 2022. The cause of this reduction in productivity is unclear but may be due to either increased freshwater inundation during the wet season, or differences in flight paths and conditions that led to more limited sampling of mangrove shrublands during October 2022. If the first explanation was the cause, we would likely have also seen an effect in mangrove scrub fluxes. Mangrove shrublands contributed half as much to the total cumulative flux footprints during October 2022 as the other deployment periods, making it difficult to rule out sampling bias. A single flight on October 17, 2022, comprised half of the sampled mangrove shrublands (Table S1). This particular flight resulted in a uniquely low estimate for the CO_2 fluxes for mangrove shrublands (Table S2). If this flight were omitted from the October 2022 mangrove shrubland disaggregation calculation, the average CO_2 for this vegetation class during October 2022 would be -8 ± 4 μmol m^{-2} s^{-1}, similar to the estimates for the other sampling periods.

Measured CH_4 fluxes likely integrate contributions of water-atmosphere fluxes from mangrove tidal creeks and sediment-atmosphere fluxes. Insignificant CH_4 emissions were measured for mangrove forests except during the October 2022 (end of wet season) period of high inundation, when average CH_4 fluxes were 29 ± 16 nmol m^{-2} s^{-1} (Fig. 6, lower panel). Fluxes from mangrove scrubs and shrublands were also higher in October 2022, though these areas tended to have larger dry-season CH_4 fluxes, ranging from 8 to14 nmol m^{-2} s^{-1} among mangrove scrub and from -4 to 9 nmol m^{-2} s^{-1} for mangrove shrublands. Rosentreter et al. (2018a) observed a similar range of 0.5—12 nmol m^{-2} s^{-1} (40—1000 µmol m^{-2} d^{-1}) water-atmosphere exchange from flux chambers at three sites in Australia, with the highest fluxes during the wet season. Much larger fluxes from mangrove soils of 110 ± 180 nmol m^{-2} s^{-1} (150 ± 250 mg m^{-2} d^{-1}) were observed during the wet season in India (Jha et al., 2014), and CH_4 fluxes from soils ranged from 0.02 to 88 nmol m^{-2} s^{-1} at four mangrove sites in Taiwan (Lin et al., 2020). There is a large variability of CH_4 emissions from mangrove waters and soils that have been reported, with an estimated global average of 3.9 ± 1.2 nmol m^{-2} s^{-1} (339 ± 106 µmol m^{-2} d^{-1}) (Rosentreter et al., 2021).

Mangrove ghost forests predictably did not take up CO_2. In these areas there had been a high tree mortality rate and massive defoliation post-Irma, without signs of recovery three years post-storm (Xiong et al., 2022). CO_2 exchange was not statistically different from zero during the first three deployment periods, but ghost forests served as a small source of CO_2 (1.1 ± 0.8 µmol m^{-2} s^{-1}) during April 2023. It should be noted that during this deployment period we more heavily targeted ghost forests, particularly during the flight on April 18, 2023 (Table S1). Ghost forests were a methane source across all deployment months, particularly during October 2022 when we observed an average emission rate of 51 ± 27 nmol m^{-2} s^{-1}. During this period ghost forests emitted more CH_4 than any of the intact mangrove areas. Higher CH_4 emissions and eliminated CO_2 uptake from ghost forests highlights the importance of mangrove preservation for mitigation of carbon emissions, and the potential for additional GHG emissions as hurricanes and coastal development continue to threaten mangrove communities globally. This is particularly significant in south Florida mangrove communities, given the high tropical storm recurrence frequency in this region and the significant impacts of past hurricanes on forest structure and productivity (Danielson et al., 2017; Rivera-Monroy et al., 2019; Lagomasino et al., 2021; Xiong et al., 2022; Chavez et al., 2023).

Saltwater Marshes

Average daily NEE for saltwater marshes ranged from -6 to -12 µmol m^{-2} s^{-1} with no statistically significant seasonality. Similar fluxes of -6.7 ± 5.5 µmol m^{-2} s^{-1} (winter—spring) and -7.9 ± 6.4 µmol m^{-2} s^{-1} were observed from an eddy-covariance tower in a tidal salt marsh in Brazil (Souza et al., 2022). An NEE range of -5 to -15 µmol m^{-2} s^{-1} was also recorded at a subtropical estuarine marsh in Taiwan (Lee et al., 2015).

CH_4 fluxes from saltwater marshes were insignificant, except during February 2023, when CH_4 fluxes were -11 ± 4 nmol m^{-2} s^{-1}. Saline marshes typically emit less CH_4 than freshwater marshes because sulfate reduction dominates over methanogenesis during decomposition of organic matter (Bartlett et al., 1987). Low methane emission fluxes of 0.08 ± 0.02 nmol m^{-2} s^{-1} (0.04 ± 0.01 g m^{-2} yr^{-1}) have also been observed in a tropical region of northwest Australia (Iram et al., 2021). In general, a large range of methane emissions from salt marshes has been observed globally (-1 to 1090 nmol m^{-2} s^{-1}, -92 to 94,000 µmol m^{-2} d^{-1}), with an estimated average of 2.6 nmol m^{-2} s^{-1} (224 µmol m^{-2} d^{-1}) (Al-Haj and Fulweiler, 2020).

The reason for the different net CH_4 and CO_2 fluxes during each deployment is not immediately obvious. Methane and CO_2 soil respiration fluxes in salt marshes are known to be influenced by tidal cycles (Kristensen et al., 2008; Rosentreter et al., 2018c; Iram et al., 2021) and it is possible that our flight data were skewed by sampling different tidal regimes. Methane uptake due to increased oxidation by methanotrophic bacteria has also been observed during the dry season of a coastal wetland in China (e.g. Hao et al., 2020). It is possible that abnormally low rainfall during February 2023 in southwest Florida contributed to the more significantly negative methane fluxes during this period.

Freshwater Marshes and Swamplands

Freshwater marshes, swamp forests, swamp scrub, and swamp shrublands are all considered freshwater wetlands. Their different classifications reflect differences in vegetation composition and distribution, with a higher percentage of tall tree cover for swamp forests and a higher percentage of grasses in freshwater marshes (Section S3). The Shark River Slough, Taylor Slough, and several other sloughs that flow through the Big Cypress Swamp connect these areas with the saltwater tidal wetlands. CO_2 uptake fluxes were relatively low over freshwater marshes (-2.9 to -3.6 µmol m^{-2} s^{-1}), with a weak seasonality. Similar daily peak fluxes for two freshwater marsh sites in ENP were observed using chamber measurements in 2008–2009 (Schedlbauer et al., 2012). The relatively low CO_2 fluxes for freshwater marshes are likely due to the lower LAI and biomass for grasses than for regions containing larger shrubs and trees (Fig. 6, Fig S17, Fig S18). Inundation also plays a significant role in these systems, causing a decline in photosynthesis with increasing length of flooding (Zhao et al., 2021). CO_2 fluxes in swamp shrublands were larger than in freshwater marshes, with a weak seasonality. These areas consist of a variety of evergreen tree species in a matrix of grasses (Supplementary Information Section S3). Average fluxes to swamp shrublands were more uncertain in April 2023, likely due to less area sampled than during other deployment periods (Table S1).

Many of the freshwater wetland regions of the Everglades, particularly freshwater marshes and swamp shrublands, contain periphyton mats in the water. These periphyton mats grow during the wet season and during periods of inundation, when they are active in fixing CO_2 from the atmosphere as calcium carbonate (Schedlbauer et al., 2012). The balance of CO_2 uptake from plant and periphyton communities, CO_2 emission from soils and waters, and the effect of inundation on these processes likely drives observed temporal changes in CO_2 exchange.

CO_2 fluxes from swamp forests were largest during April 2022 and April 2023 (-10 ± 5 µmol m^{-2} s^{-1} and -10 ± 4 µmol m^{-2} s^{-1}, respectively), during the dry- to wet-season transition period, with much smaller fluxes observed during October 2022 and February 2023 (-4 ± 2 µmol m^{-2} s^{-1} and -3 ± 2 µmol m^{-2} s^{-1}, respectively) when the sun was lower and temperatures were cooler. Similar seasonality can be seen for swamp scrub. Swamp forests and swamp scrub vegetative regions are dominated by deciduous bald cypress trees (Ruiz et al., 2021). The majority of these conifers were observed to either lack leaves or had brown needles during October and February flights.

CH_4 emissions were largest for freshwater marshes and swamp shrublands, with the largest emissions in October 2022 during the tail end of the wet season when soils were inundated. Average October 2022 fluxes for freshwater marshes, swamp forests, swamp scrubs, and swamp shrublands were 59 ± 26 nmol m^{-2} s^{-1}, 52 ± 24 nmol m^{-2} s^{-1}, 33 ± 18 nmol m^{-2} s^{-1}, and 69 ± 29 nmol m^{-2} s^{-1}, respectively. Much larger CH_4 fluxes of 42–1200 nmol m^{-2} s^{-1}, (44–1244 mg C-CH_4 m^{-2} d^{-1}) have been recorded in both marsh and forested wetland areas of Veracruz, Mexico (Marín-Muñiz et al., 2015) and Costa Rica (Nahlik and Mitsch 2011). More comparable CH_4 emission rates of 48–290 nmol m^{-2} s^{-1} (0.05—0.3 g C-CH_4 m^{-2} d^{-1}) during periods of inundation, and 2 ± 1 nmol m^{-2} s^{-1} (0.002 ± 0.001 g C-CH_4 m^{-2} d^{-1}) during dry conditions were recorded from an eddy flux tower in the Pantanal wetland of Brazil (Dalmagro et al., 2019). Recently, Murguia-Flores et al. (2023) identified a median (IQR) CH_4 emission rate for tropical shallow-water inland wetlands of 39.2 (7.1–180.7) nmol m^{-2} s^{-1}, or 40.6 (7.4–187.3) g C-CH_4 m^{-2} d^{-1}. Our measurements from freshwater wetlands in southern Florida fall within this range and close to the reported median.

Upland Woodlands

Upland woodlands exhibited a moderately high NEE ranging from -4 to -8 μmol m^{-2} s^{-1}. A similar range (-6 to 12 μmol m^{-2} s^{-1}) of NEE for slash pine plantations in subtropical Australia was also observed across wet and dry seasons (McGowan et al., 2020). This vegetation region also demonstrates a similar but less pronounced seasonal cycle of CO_2 fluxes as swamp forests. Although most of the upland woodlands in this region are dominated by evergreen slash pine, this seasonality may be caused by variations in PAR and by the presence of some semi-deciduous species, such as laurel oaks. It is also possible that the productivity of flood-intolerant upland woodland species was somewhat suppressed during October 2022 at the tail of the wet season when water levels were relatively high (Fig S17). Reduction of NEE for October 2022 could have also been driven by increased soil respiration during the wet season when soil moisture was higher (Fig S17), (Orchard and Cook 1983, Hawkes et al., 2016).

Methane fluxes from upland woodlands were undetectable in April 2022, and were slightly negative at -9 ± 4 nmol m^{-2} s^{-1} and -9 ± 5 nmol m^{-2} s^{-1} for February 2023 and April 2023, respectively. Similar negative fluxes have also been observed during the dry season in tropical upland forests in Costa Rica (Nahlik and Mitsch, 2011) and in the Amazon (Gauci et al., 2024). In contrast, a large positive flux of methane (40 ± 19 nmol m^{-2} s^{-1}) was observed during October 2022. Wet season methane emissions have been observed in upland regions of tropical and subtropical regions elsewhere, when upland forests and woodlands can switch from being a methane sink to a methane source (Megonigol and Guenther, 2008).

3.2.2 Other surface properties

Within each vegetation land classification, there still exists substantial surface heterogeneity. For example, comparing the extent of mangrove forests (Fig. 2) with the maps of observed fluxes (Fig 5), it is apparent that this ecosystem exhibits a range of midday fluxes, even within the same month. The interquartile range of CO_2 fluxes observed where the footprint consists of 80% mangrove forest is -15.1 to -6.5 µmol m^2s^{-1} during April 2022. Similarly, the interquartile range of CH_4 fluxes observed where the footprint consists of 80% freshwater marsh is 13 to 73 nmol m^2 s^{-1} during April 2022. Vegetation type alone explains 35 - 53% of variability in observed fluxes (Fig S16). Variability in the underlying drivers of CO_2 and CH_4 exchange within an ecosystem type also influences heterogeneity in fluxes. For example, the range of LAI for footprints containing 80% or more mangrove forests in April 2022 was 1.9 to 6.3 m^2/m^2 and the range of canopy heights was 5–20 m. For footprints containing 80% or more freshwater marsh in October 2022, the range of water depths was 6–97 cm.

Table 1: Spearman's correlation coefficients for CO_2 and CH_4 fluxes and surface properties.

Data set	CO_2 all	CO_2 mangrove[a,b]	CH_4 all	CH_4 freshwater marsh[a]
LAI	-0.52	-0.36	-0.16	-0.02
FPAR	-0.52	-0.39	-0.07	0.07
EVI	-0.51	-0.51	-0.23	-0.17
NDVI	-0.46	-0.51	-0.14	0.06
Canopy Height	-0.35	-0.54	-0.33	-0.11
AGBM	-0.35	-0.54	-0.27	-0.13
Soil moisture	0.17	0.05	0.27	0.16
water depth	0.18	-0.33	0.53	0.44
PAR	-0.14	0.03	-0.10	-0.11
VPD	-0.32	-0.12	-0.02	-0.07
T	-0.06	0.02	-0.05	0.13
RH	0.25	0.12	-0.02	0.15

a. *Considering footprints consisting of more than 80% of the given land type.*
b. *All mangrove ecosystems (forest, shrubland, scrub) are combined.*

Spearman's correlation coefficients between 1 km averaged GHG fluxes and a variety of surface and atmospheric variables are shown in Table 1. For surface data sets (LAI, FPAR, EVI, NDVI, Canopy Height, AGBM, soil moisture, and water depth) correlation coefficients are calculated between GHG fluxes and footprint weighted variables. Vapor pressure deficit (VPD), temperature (T), and relative humidity (RH) are based on airborne temperature and water vapor measurements. Photosynthetically active radiation (PAR) was estimated from the NOAA High-Resolution Rapid Refresh (HRRR) Model product at 3 km resolution interpolated to the 1 km averaged flight tracks. Spearman's correlation coefficients were used over Pearson's coefficients because many of the relationships between the environmental and surface variables are non-linear (Fig. 7, Fig 8).

The strongest predictors of CO_2 fluxes for all flux data were LAI and FPAR (Table 1, Fig 7). However, within mangrove ecosystems (forest, shrublands, and scrub), canopy height and above ground biomass had the most robust relationship with CO_2 fluxes. In contrast, CH_4 fluxes over all flight tracks and over freshwater marshes both correlate best with EDEN water depth (Table 1, Fig 8). The largest CH_4 fluxes and EDEN water depths were over water management regions outside of ENP or BCNP boundaries (Fig 3, Fig 5, Fig S17). The influence of water on the methane emissions is not surprising, as numerous studies have observed larger methane emissions in coastal wetlands during the wet season when soils are inundated and conditions in the soil become more anaerobic and ideal for methanogenesis (e.g. Nahlik and Mitsch 2011; Beringer et al., 2013; Marín-Muñiz et al., 2015; Dalmagro et al., 2019; Hondula et al., 2021). This relationship confirms that higher CH_4 fluxes during October 2022 were likely due to inundation. This flight period occurred following Hurricane Ian. Analysis of EDEN water data sets since 2002 suggests that water levels were slightly elevated relative to the October average, but comparable to many other years on record (Fig S19).

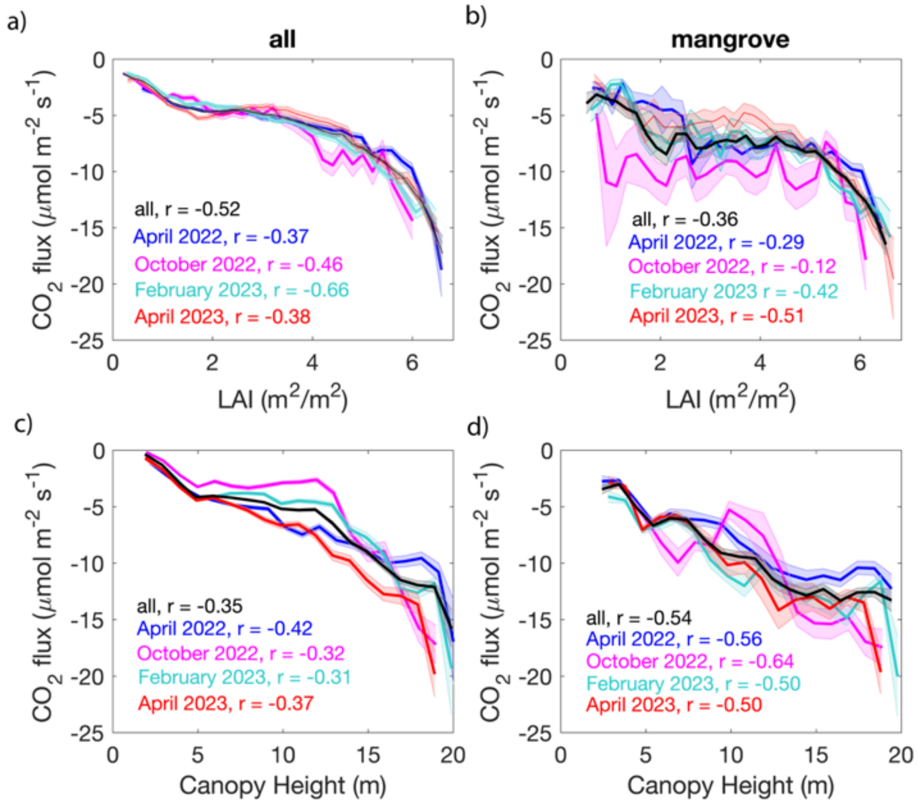

Figure 7: Relationships between CO_2 flux and leaf area index (LAI) (**a, b**) and between CO_2 flux and Canopy Height (**c, d**) for all 10 second averaged data (**a, c**), and for data where footprints were comprised of 80% mangroves (mangrove forests, mangrove shrublands, and mangrove scrubs) (**b, d**). CO_2 data are averaged over 0.25 $m^2\ m^{-2}$ LAI bins or 2 m canopy height bins. Solid black, blue, magenta, turquoise, and red lines are the average for all flights, April 2022, October 2022, February 2023, and April 2023, respectively. Shaded areas are the 95% confidence interval of the mean.

Interestingly, we observe a slightly negative relationship between VPD and CO_2 flux. This is likely both due to the generally high humidity and water availability in the region (50—90%) and because VPD was higher during the April months when there was greater sunlight availability and the deciduous bald cypress trees were green. Similar relationships between VPD and mangrove NEE have also been reported for mangroves in the Yucatan (Alvarado-Barrientos et al., 2020).

Some relationships between fluxes and environmental variables likely come about because of redundant and non-causational correlations. For example, the negative relationship between canopy height and CH_4 fluxes, are likely due to correlations between surface variables. In this case, greater canopy height does not cause lower CH_4 emissions, but areas with greater canopy heights are often mangrove forests and areas with less surface water extent where there are low CH_4 emissions. Many of the variables tested, such as EVI, NDVI, Canopy Height, LAI, and AGBM also co-vary with each other.

The relationships between remotely sensed vegetation and soil properties and carbon fluxes demonstrate the potential predictive power of remote sensing for greenhouse gas fluxes. Incorporation of remotely sensed data sets into a predictive machine learning model of southern Florida CO_2 and CH_4 fluxes is a part of ongoing work.

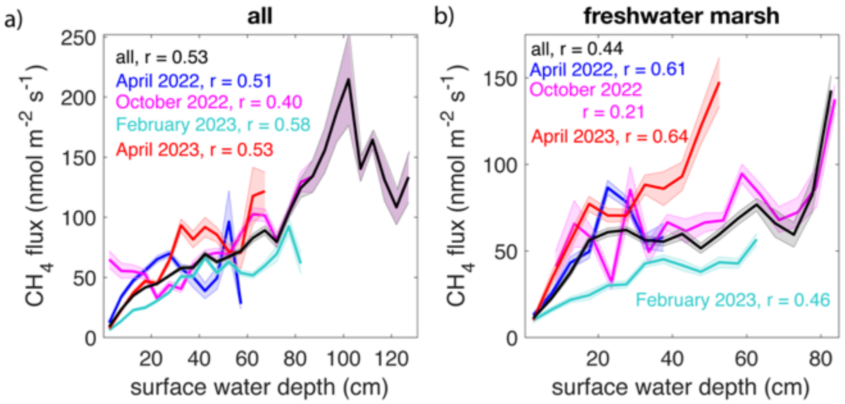

Figure 8: Relationships between CH_4 flux and EDEN surface water depth all 10 second averaged data (**a**), and for data where footprints were comprised of 80% freshwater marsh (**b**). CH_4 fluxes are averaged over water depth in 5 cm bins. Solid black, blue, magenta, turquoise, and red lines are the average for all flights, April 2022, October 2022, February 2023, and April 2023, respectively. Shaded areas are 95% confidence intervals. All 10-second averaged data include areas outside of the national park boundaries where vegetation data area available.

3.3 Flux tower comparisons

Comparison of airborne fluxes to EC flux tower measurements requires careful consideration of flux footprints (Hannun et al., 2020). Only one flight had a flux footprint that directly overlapped with the mangrove forest tower site (SRS-6) while that tower site was active, and measurements only overlapped for several seconds, making a direct comparison with the flux towers impossible. Indirect comparison of airborne and EC tower fluxes is complicated by surface variability and resulting heterogeneity of fluxes. Each airborne flux footprint typically consisted of several vegetation types and a further range of surface properties (LAI, canopy heights, soil moisture, surface water extent, etc.). In contrast, the EC tower footprints typically covered only single ecosystem type with greater homogeneity.

We indirectly compare the average monthly fluxes of CH_4 and CO_2 from eddy covariance tower ground sites (when available) to airborne flux measurements with footprints consisting primarily of similar surface properties as the ground sites. Airborne CO_2 and CH_4 fluxes were averaged over all flight days during a given month after selecting for data that met certain criteria for comparison with the EC tower. For CH_4 flux comparisons with SRS-2 and TS/Ph-1, airborne data were filtered to only include points where freshwater marsh constituted more than 80% of the footprint and the footprint weighted average water depth was within 10 cm of the EC tower for the given month (Table S6). For SRS-6 comparison, airborne fluxes were included in the average if footprints contained more than 80% mangrove forest. Airborne CO_2 fluxes were averaged during each flight day where footprints constituted over 80% of the EC tower land classification and had a footprint weighted LAI within 1 m^2/m^2 of the EC tower footprint LAI for the given month (Table S7). EC tower fluxes were averaged for all available data during a given month from 10:00—17:00 local time (LT).

Comparisons indicate relatively good agreement between EC flux tower and airborne flux measurements (Fig. 9). These comparisons provide a validation of our airborne CWT fluxes, as well as confirm that surface water extent, LAI, and vegetation class indeed capture much of the observed variability in carbon exchange. Tower comparisons with latent heat (LE) and sensible heat (H) are discussed in Supplementary Information section S4 and Figures S6-S8.

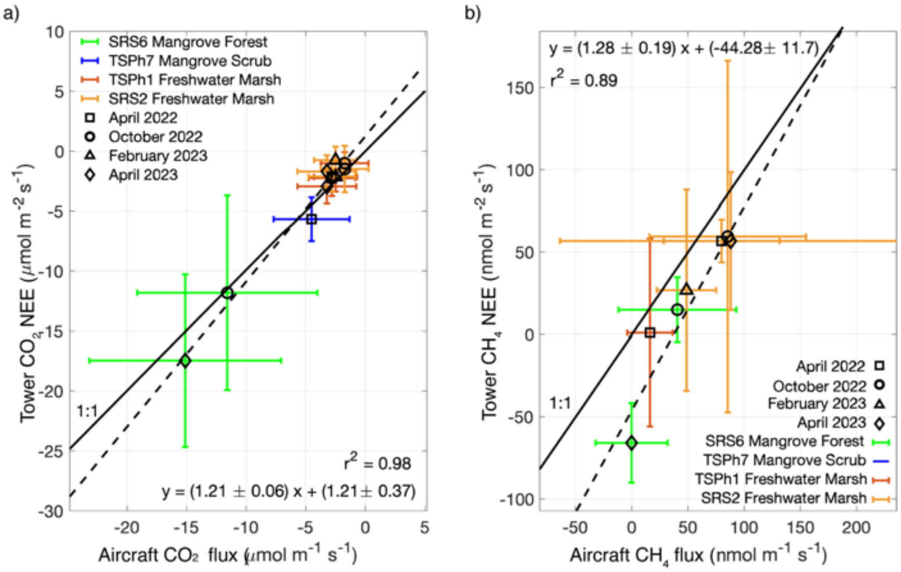

Figure 9: Comparison of EC fluxes from flux tower sites with airborne fluxes measured from the King Air for a) CO_2 and b) CH_4. EC tower CH_4 and CO_2 NEE (flux – storage) for a given month were averaged over all available data between 10:00 and 16:00 LT. Airborne CH_4 fluxes were averaged over all flight days for data with the same vegetation class and surface water as the EC tower. Airborne CO_2 fluxes were averaged during each flight day after filtering data for the same vegetation class and LAI as the EC tower. EC towers SRS-6, SRS=2, TS/Ph-1, and TS/Ph-7 sample mangrove forest, freshwater marsh, freshwater marsh, and mangrove scrub, respectively. Error bars are one standard deviation. The dashed line is the 1:1 line.

3.4. Estimates of net carbon fluxes

The balance between CH_4 emissions and CO_2 uptake partially determines the impact of wetland ecosystems on carbon sequestration and climate change mitigation. To estimate the net impact of the entire Everglades region on carbon exchange during our sampling periods, we first scaled CH_4 fluxes by their CO_2 equivalent global warming potential (GWP) using a factor of 27.9 g CH_4/g CO_2 in accordance with the latest IPCC report (Forster et al., 2021) and then calculated the net CO_2 equivalent exchange rate and the fraction of total CO_2 uptake that is offset by CH_4 emissions for each vegetation region based on disaggregated fluxes. These values were then scaled by the total area of each vegetation region adequately sampled in ENP and BCNP (Fig. S20, Fig. S21). During daytime sampling periods, the 6,237 km^2 area of south Florida represented by the sampled land classes has a total CO_2 equivalent exchange rate of -5.3 ± 2.6 to -2.7 ± 1.5 Gg CO_2 hr^{-1}, with CH_4 emissions offsetting CO_2 by 3 ± 1% to 14 ± 4 %, depending on the month. The largest CH_4 emissions relative to CO_2 uptake occurred during the October 2022 deployment (Fig. S21). However, midday airborne flux measurements do not include nighttime CO_2 respiration which is required for an estimate of daily carbon exchange.

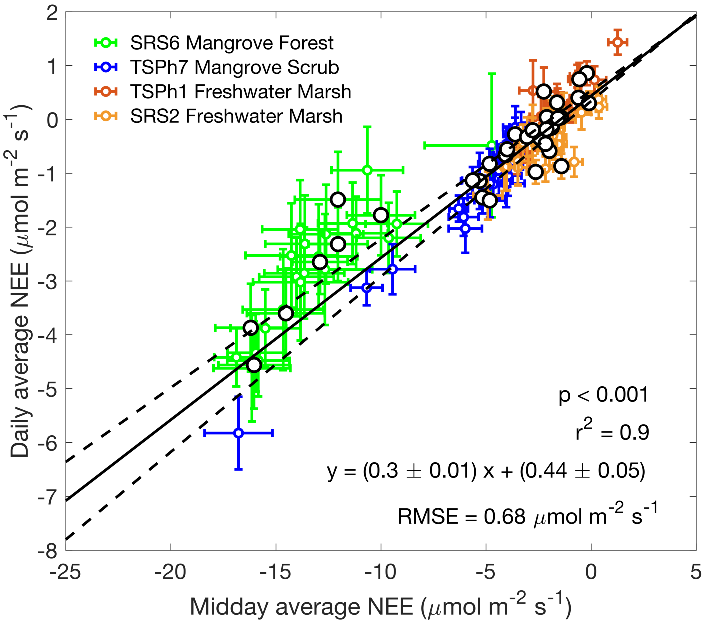

Figure 10: Linear fit of daily 24 hr average net ecosystem exchange (NEE) and the average daytime NEE between LT 10:00 and 17:00 for all tower sites in the flight domain. Each marker represents a monthly average from data available between 2020 and 2023. Larger black markers are monthly averages during April, February, and October. The line of best fit and the 95% confidence interval are solid and dotted lines, respectively. Error bars are 1σ.

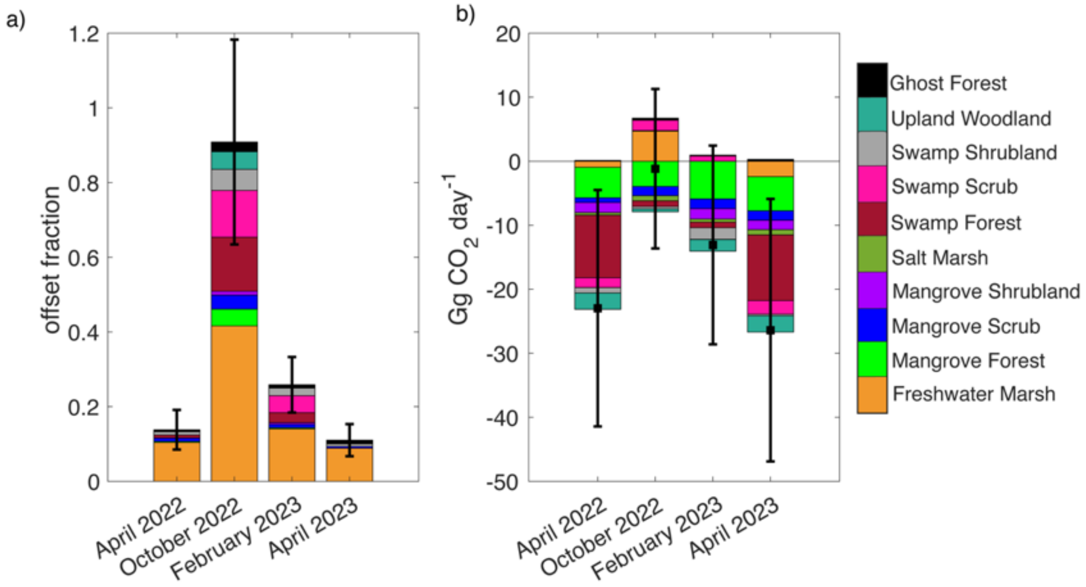

Figure 11: (**a**) GWP-scaled CH_4 emissions as a fraction of the CO_2 uptake for each month across the BlueFlux experimental domain. Colors indicate the contribution of each ecosystem classification. CH_4 offset fractions are weighted by the area of each ecosystem type. (**b**) Average daily net CO_2 equivalent uptake for each deployment period, calculated as the sum of CO_2 and GWP-scaled CH_4 fluxes. Total daily CO_2 fluxes were calculated by from the daytime airborne measurements using the linear fit of daily integrated NEE and daytime NEE from Figure 10. CH_4 fluxes were assumed to be constant throughout the day so average disaggregated CH_4 fluxes for each deployment period were scaled by 24 hours. Ecosystem contributions are scaled by area. Error bars are 1σ.

Tower flux observations constrain the diurnal cycle of carbon exchange in several locations. We use this diurnal temporal information from the Everglades tower network to extrapolate daytime fluxes (LT 10:00–17:00) to total daily carbon exchange in ENP and BCNP as in Hannun et al. (2020) (Figure S22). The tower sites in the BlueFlux/FCE LTER domain are located in three different vegetation regions that represent the three dominant vegetation types, including tall riverine mangrove forests (SRS-6), scrub mangroves (TS/Ph-7), and freshwater marshes (SRS-2 and TS/Ph-1). These tower sites demonstrate a linear relationship between the total CO_{2}- NEE between LT 10:00 and 17:00 and the total daily integrated NEE (Fig. 10, r = 0.94). A similar relationship was also derived for EC tower sites in the mid-Atlantic region over several different ecosystem types (Hannun et al., 2020). We scale the average ecosystem CO_2 fluxes measured by CARAFE during LT 10:00–17:00 (Fig. 6) by the relationship shown in

Figure 10 to estimate the 24 hr average NEE for each vegetation class during the months of our flight measurements.

The CH_4 average midday flux measured by the tower sites was not significantly different from the daily average (Figure S23). Thus, CH_4 fluxes are treated as constant throughout the day and average daytime CH_4 fluxes were assumed to be representative of daily averaged fluxes.

Figure 11 shows the resulting daily CH_4 offsets to CO_2 uptake and net daily CO_2 equivalent exchange for each deployment period across ENP and BCNP. CH_4 emissions relative to CO_2 uptake are lowest during April 2023, with CH_4 emissions offsetting 11 ± 4 % of CO_2 uptake and a total net carbon exchange rate of -26 ±20 Gg CO_2-eq d^{-1}. The largest CH_4 emissions relative to CO_2 uptake are during October 2022, with CH_4 emissions offsetting 91 ± 27% of CO_2 uptake and a net carbon exchange rate of -1 ± 12 Gg CO_2-eq d^{-1}. This range of uncertainty in the. net carbon exchange is large, and as such the region may either serve as a net source or net sink of carbon during October. The largest source of CH_4 emissions relative to CO_2 uptake are the freshwater marshes, particularly during the October 2022 wet season, when we estimate that they serve as a 5 Gg CO_2-eq d^{-1} source of carbon. Mangrove forests contribute a relatively small amount of CH_4 emission and provide the largest net sink of carbon cumulatively across all deployment periods with an average net carbon flux of -5 ± 2 Gg CO_2-eq d^{-1}. Swamp forests provide the largest net carbon sink during the dry/growing season (almost double than that of mangroves), as observed during April 2022 and April 2023.

Carbon exchange in southern Florida wetlands exhibits strong seasonality over the measurement period, with the ENP and BCNP region potentially serving as a net source of carbon to the atmosphere during the wet season and periods of high inundation. Mangrove and cypress swamp forests are large atmospheric sinks of carbon for the region, despite their relatively small extents. The importance of cypress swamp forests in CO_2 removal is likely even greater than this study reflects, as we do not have measurements in the summer when leaf area is at a peak.

The uncertainty in our estimates of daily carbon balance over ENP and BCNP is large, as it includes the propagated uncertainty in the net monthly fluxes due to variability within an ecosystem type (i.e due to LAI, water depth, soil moisture, tidal cycles, temperature, salinity, effects of recent hurricanes and recovery, etc), uncertainty in airborne fluxes, uncertainty in the disaggregation of fluxes, and uncertainty in the diurnal upscaling. However, these results serve as a first EC-based estimate of net carbon fluxes over the entire Everglades and Big Cypress area and are demonstrative of the temporal differences in carbon exchange across the region during different months, as well as the potetial importance of the different vegetation regions in the carbon balance.

There are several additional limitations to this diurnal upscaling analysis that should be noted. Each tower only covers an extremely limited area within an ecosystem type, while the data sampled from the flights includes a much larger range of conditions and surface variability (LAI, canopy height, water depth, tidal influences, salinity, etc.). We have thusly chosen to use a uniform diurnal scaling factor for each vegetation type rather than a separate tower-derived relationship for mangrove forests, mangrove scrub, and freshwater marshes as we believe it to be more representative of the observed variability of conditions throughout our flight domain.

Results using a distinct relationship for mangrove forests, mangrove scrub, and freshwater marshes can be found in Figure S24.

The domain of swamp forests, swamp scrubs, and upland woodlands were outside the tower FCE LTER study area, and are not represented in deriving the diurnal upscaling relationship. Eddy covariance flux tower measurements conducted in BCNP during 2012—2014 measured average CO_2 NEE of -108 ± 5 g C m^{-2} $month^{-1}$, -48 ± 3 g C m^{-2} $month^{-1}$, and -68 ± 5 g C m^{-2} $month^{-1}$ during April months at a cypress swamp (swamp forest), dwarf cypress (swamp scrub), and pine upland (upland woodland) site, respectively (Shoemaker et al., 2015). We obtain lower average estimates for these vegetation areas during our 2022—2023 April deployments of -85 ± 40 g C m^{-2} $month^{-1}$, -16 ± 10 g C m^{-2} $month^{-1}$, and -51 ± 30 g C m^{-2} $month^{-1}$, respectively, when scaling using the relationship derived in Figure 10. While the 2012–2014 tower measurements for swamp forests and upland woodlands are within the range of uncertainty of our estimates, the tower measurement from the swamp scrub site is not. It is not clear if this difference is due to error in our analysis, the decade long separation between tower and flight measurements, or flux variability over this ecosystem type not captured by the tower.

It should also be noted that in tidal wetland regions like the Everglades, the net ecosystem carbon balance is affected by lateral aqueous transport of carbon in addition to NEE (Troxler et al., 2013). Carbon initially taken up in one area may be stored in above and below ground biomass, soils, and sediments, or it may laterally flow from the area of initial uptake to later be reemitted or stored in soils and sediments downstream (Bouillon et al., 2008; Alongi and Mukhopadhyay, 2015; Rosentreter et al., 2018b). Aquatic lateral transport in the Everglades has been estimated to be relatively small (~10%) compared to the NEE of mangrove forests (Troxler et al., 2013). However, freshwater marshes in the Everglades store a substantial amount of carbon (400-650 g C m^{-2} yr^{-1}), with almost all the carbon input through aqueous lateral transport (Troxler et al., 2013). In this study we discuss the net vertical carbon exchange largely from an atmospheric perspective, but it should not be taken as the complete story of carbon storage in the Everglades.

5 Conclusions

Airborne eddy covariance with continuous wavelet transforms can resolve heterogenous fluxes over a diverse mosaic of ecosystems across the coastal landscape of southern Florida. The largest CO_2 uptake fluxes were observed during April 2022 and 2023 over cypress swamp forests and over mangrove forests during all sampling periods. During the tail-end of the wet season and near maximum water levels (October 2022 campaign), we observed the largest CH_4 emission fluxes from all vegetation types. Across all deployments, we recorded the largest CH_4 fluxes from freshwater marshes and freshwater swamp shrublands. Additionally, we see some evidence for CH_4 uptake during the dry season in salt marshes and upland forests. Upscaling average ecosystem fluxes over the sample domain, we estimate average net CO_2-eq fluxes of -4 ± 3 g CO_2-eq m^{-2} d^{-1} in April and -0.2 ± 2 g CO_2-eq m^{-2} d^{-1} in October (area-integrated rates of -26 ±20 Gg CO_2-eq d^{-1} and -1 ± 12 Gg CO_2-eq d^{-1}, respectively).

Our findings highlight the role of freshwater swamp forests and mangrove forests as extremely productive coastal ecosystems. Observed rates of CO_2 uptake and CH_4 emission for these ecosystems fall within the range of observations for mangroves and swamp forests in similar subtropical and tropical regions globally. Results support the importance of these ecosystems as important carbon stores and the potential for additional GHG emissions resulting from hurricanes, coastal development, and hydrological management. However, the diversity and vulnerability of these ecosystems necessitates continued ongoing research into the carbon storage potential and the effects of restoration and degradation on the role of swamp and mangrove forests in the global coastal carbon cycle.

Combined with landcover information like vegetation type, leaf area, canopy height, vegetation indices, and surface water depth, airborne fluxes can help elucidate the underlying causes of the observed variability in carbon fluxes. In particular, surface water depth in the freshwater wetlands was strongly positively correlated with CH_4 emissions. In a heavily water managed area like southern Florida, policy decisions related to agriculture and hydrology may overlap with greenhouse gas reduction strategies. Moreover, the ongoing large-scale hydrological restoration of the Greater Everglades under the Comprehensive Everglades Restoration Plan (CERP) will likely have significant effects on vegetation dynamics, especially carbon storage and sequestration potential, thereby influencing the role of wetlands in climate change mitigation and adaptation. The relationship between surface water and methane emission in this study relied heavily on the long-term Everglades Depth Estimation Network data set. However, such high-resolution surface information is currently extremely limited globally. Improvements in high resolution remotely sensed soil moisture and surface water data will be critical for ongoing research into relationships between regional hydrology and global methane emissions. Other surface information, such as high-density coastal wetland salinity maps, would also be beneficial to this analysis.

A limitation of this study is the lack of observations during the peak of the wet season (May-September). Additional airborne flux measurements in southern Florida are needed to better constrain seasonality (particularly wet-season fluxes), diurnal cycles, and tidal influences. These efforts would improve the ongoing carbon budget analysis of coastal wetlands in the Everglades region and add an understanding of the carbon sink and source capacity of these ecosystems exposed to increasing impacts of sea-level rise and climate change.

The importance of vulnerable coastal wetland ecosystems to the CO_2 and CH_4 global budgets highlights the need for continued and sustained measurements in these regions. Airborne eddy covariance, especially paired with remote-sensing surface information, represents a powerful tool for constraining biogenic carbon cycles.

Acknowledgments

We acknowledge Michael Bonsteel, Irene Romero, Tonya Howington, and Steve Schulze for assistance with National Park permitting. We thank Dynamic Aviation Group Inc. and especially Clay King, Kris Estrep, and Ethan Pearce for their support and flexibility. We gratefully acknowledge the pilots who flew in the BlueFlux mission and were critical for obtaining this data set: Lawrence Grippo, Dustin Hill, Stephen Bielick, Nathan Bierman, Benjamin Powell, and

Ryan Kelley. We also thank Bruce Woodcock at Aventech for his assistance in analyzing the winds data from the AIMMS-20 probe. We acknowledge and respect the Indigenous peoples of the Florida Everglades, including the Miccosukee and Seminole Tribes, on whose ancestral lands this research takes place. The BlueFlux mission was supported by the NASA Carbon Monitoring System Solicitation No. NNH20ZDA001N-CMS. ERD was supported by the NASA Postdoctoral Program sponsored by the National Aeronautics and Space Administration (NASA) through a contract with ORAU. Funding for SRS-6, and TS/Ph-7 tower sites is provided by the National Park Service through Cooperative Agreements No. P16AC00032 Task Agreement No. P17AC01282. Towers at SRS-2 and TS/Ph-1 were supported by the National Science Foundation Division of Atmospheric and Geospace Sciences (award 1561139 and 1807533), and the National Science Foundation Graduate Research Fellowship Program (Fellow No. 2023348536). This is contribution #1773 from the Institute of Environment at Florida International University. We would also like to thank the two reviewers for their constructive comments and advice in improving this manuscript.

Open Research

The airborne data used for all analysis in the study (concentrations, fluxes, meteorology, and aircraft navigational parameters) are openly available at ORNL DAAC via DOI:10.1126/science.216.4547.733 (Delaria et al., 2024).

References

Adame, M. F., Connolly, R. M., Turschwell, M. P., Lovelock, C. E., Fatoyinbo, T., Lagomasino, D., Goldberg, L. A., Holdorf, J., Friess, D. A., Sasmito, S. D., Sanderman, J., Sievers, M., Buelow, C., Kauffman, J. B., Bryan-Brown, D., & Brown, C. J. (2021). Future carbon emissions from global mangrove forest loss. Global Change Biology, 27(12). https://doi.org/10.1111/gcb.15571

Al-Haj, A. N., & Fulweiler, R. W. (2020). A synthesis of methane emissions from shallow vegetated coastal ecosystems. In Global Change Biology (Vol. 26, Issue 5). https://doi.org/10.1111/gcb.15046

Alongi, D. M., & Mukhopadhyay, S. K. (2015). Contribution of mangroves to coastal carbon cycling in low latitude seas. Agricultural and Forest Meteorology, 213. https://doi.org/10.1016/j.agrformet.2014.10.005

Alvarado-Barrientos, M. S., López-Adame, H., Lazcano-Hernández, H. E., Arellano-Verdejo, J., & Hernández-Arana, H. A. (2021). Ecosystem-Atmosphere Exchange of CO2, Water, and Energy in a Basin Mangrove of the Northeastern Coast of the Yucatan Peninsula. Journal of Geophysical Research: Biogeosciences, 126(2). https://doi.org/10.1029/2020JG005811

Barbier, E. B., Hacker, S. D., Kennedy, C., Koch, E. W., Stier, A. C., & Silliman, B. R. (2011). The value of estuarine and coastal ecosystem services. In Ecological Monographs (Vol. 81, Issue 2). https://doi.org/10.1890/10-1510.1

Barr, J. G., V. Engel, J. D. Fuentes, J. C. Zieman, T. L. O'Halloran, T. J. Smith III, and G. H. Anderson (2010), Controls on mangrove forest-atmosphere carbon dioxide exchanges in western Everglades National Park, J. Geophys. Res., 115, G02020, doi:10.1029/2009JG001186.

Barr, J. G., Engel, V., Smith, T. J., & Fuentes, J. D. (2012). Hurricane disturbance and recovery of energy balance, CO 2 fluxes and canopy structure in a mangrove forest of the Florida Everglades. Agricultural and Forest Meteorology, 153. https://doi.org/10.1016/j.agrformet.2011.07.022

Bartlett, K. B., Bartlett, D. S., Harriss, R. C., & Sebacher, D. I. (1987). Methane emissions along a salt marsh salinity gradient. Biogeochemistry, 4(3). https://doi.org/10.1007/BF02187365

Beringer, J., Livesley, S. J., Randle, J., & Hutley, L. B. (2013). Carbon dioxide fluxes dominate the greenhouse gas exchanges of a seasonal wetland in the wet-dry tropics of Northern Australia. Agricultural and Forest Meteorology, 182–183. https://doi.org/10.1016/j.agrformet.2013.06.008

Bouillon, S., Borges, A. v., Castañeda-Moya, E., Diele, K., Dittmar, T., Duke, N. C., Kristensen, E., Lee, S. Y., Marchand, C., Middelburg, J. J., Rivera-Monroy, V. H., Smith, T. J., & Twilley, R. R. (2008). Mangrove production and carbon sinks: A revision of global budget estimates. Global Biogeochemical Cycles, 22(2). https://doi.org/10.1029/2007GB003052

Campbell, A. D., Fatoyinbo, L., Goldberg, L., & Lagomasino, D. (2022). Global hotspots of salt marsh change and carbon emissions. Nature, 612(7941). https://doi.org/10.1038/s41586-022-05355-z

Castañeda-Moya, E., Twilley, R. R., & Rivera-Monroy, V. H. (2013). Allocation of biomass and net primary productivity of mangrove forests along environmental gradients in the Florida Coastal Everglades, USA. Forest Ecology and Management, 307. https://doi.org/10.1016/j.foreco.2013.07.011

Chavez, S., Wdowinski, S., Lagomasino, D., Castañeda-Moya, E., Fatoyinbo, T., Moyer, R. P., & Smoak, J. M. (2023). Estimating Structural Damage to Mangrove Forests Using Airborne Lidar Imagery: Case Study of Damage Induced by the 2017 Hurricane Irma to Mangroves in the Florida Everglades, USA. Sensors, 23(15). https://doi.org/10.3390/s23156669

Crawford, T. L., Dobosy, R. J., McMillen, R. T., Vogel, C. A., & Hicks, B. B. (1996). Air-surface exchange measurement in heterogeneous regions: Extending tower observations with spatial structure observed from small aircraft. Global Change Biology, 2(3). https://doi.org/10.1111/j.1365-2486.1996.tb00079.x

Danielson, T. M., Rivera-Monroy, V. H., Castañeda-Moya, E., Briceño, H., Travieso, R., Marx, B. D., Gaiser, E., & Farfán, L. M. (2017). Assessment of Everglades mangrove forest resilience: Implications for above-ground net primary productivity and carbon dynamics. Forest Ecology and Management, 404. https://doi.org/10.1016/j.foreco.2017.08.009

Didan, K. (2015). MOD13Q1 MODIS/Terra Vegetation Indices 16-Day L3 Global 250m SIN Grid V006 [Data set]. NASA EOSDIS Land Processes Distributed Active Archive Center. Accessed 2023-09-10 from https://doi.org/10.5067/MODIS/MOD13Q1.006

Dalmagro, H. J., Zanella de Arruda, P. H., Vourlitis, G. L., Lathuillière, M. J., de S. Nogueira, J., Couto, E. G., & Johnson, M. S. (2019). Radiative forcing of methane fluxes offsets net carbon dioxide uptake for a tropical flooded forest. Global Change Biology, 25(6). https://doi.org/10.1111/gcb.14615

Delaria, E.R., G.M. Wolfe, R.A. Hannun, K. Blanock, B. Poulter, and K.L. Thornhill. (2024). BlueFlux Airborne Trace Gases, Fluxes, and Mixing Ratios, Southern Florida, 2022-2023. ORNL DAAC, Oak Ridge, Tennessee, USA. https://doi.org/10.3334/ORNLDAAC/2327

Desjardins, R. L., Brach, E. J., Alvo, P., & Schuepp, P. H. (1982). Aircraft monitoring of surface carbon dioxide exchange. Science, 216(4547). https://doi.org/10.1126/science.216.4547.733

Donato, D. C., Kauffman, J. B., Murdiyarso, D., Kurnianto, S., Stidham, M., & Kanninen, M. (2011). Mangroves among the most carbon-rich forests in the tropics. Nature Geoscience, 4(5). https://doi.org/10.1038/ngeo1123

Duarte, C. M. (2017). Reviews and syntheses: Hidden forests, the role of vegetated coastal habitats in the ocean carbon budget. In Biogeosciences (Vol. 14, Issue 2). https://doi.org/10.5194/bg-14-301-2017

Dubayah, R., Tang, H., Armston, J., Luthcke, S., Hofton, M., J. B. Blair (2021). GEDI L2B Canopy Cover and Vertical Profile Metrics Data Global Footprint Level V002 [Data set]. NASA EOSDIS Land Processes DAAC. Accessed 2022-11-13 from https://doi.org/10.5067/GEDI/GEDI02_B.002.

Dubayah, R. O., Armston, J., Healey, S. P., Yang, Z., Patterson, P. L., Saarela, S., Stahl, G., Duncanson, L., Kellner, J. R., Bruening, J., & Pascual, A. (2023). GEDI L4B Gridded Aboveground Biomass Density, Version 2.1. ORNL DAAC, Oak Ridge, Tennessee, USA. https://doi.org/10.3334/ORNLDAAC/2299

Finkelstein, P. L., & Sims, P. F. (2001). Sampling error in eddy correlation flux measurements. Journal of Geophysical Research Atmospheres, 106(D4). https://doi.org/10.1029/2000JD900731

Forster, P., T. Storelvmo, K. Armour, W. Collins, J.-L. Dufresne, D. Frame, D.J. Lunt, T. Mauritsen, M.D. Palmer,.M. Watanabe, M. Wild, and H. Zhang, (2021). The Earth's Energy Budget, Climate Feedbacks, and Climate Sensitivity. In Climate Change 2021: The Physical Science Basis. Contribution of Working Group I to the Sixth Assessment Report of the Intergovernmental Panel on Climate Change [Masson-Delmotte, V., P. Zhai, A. Pirani, S.L. Connors, C. Péan, S. Berger, N. Caud, Y. Chen, L. Goldfarb, M.I. Gomis, M. Huang, K. Leitzell, E. Lonnoy, J.B.R. Matthews, T.K. Maycock, T. Waterfield, O. Yelekçi, R. Yu, and B. Zhou (eds.)]. Cambridge University Press, Cambridge, United Kingdom and New York, NY, USA, pp. 923–1054, doi:10.1017/9781009157896.009.

Friedlingstein, P., O'sullivan, M., Jones, M. W., Andrew, R. M., Gregor, L., Hauck, J., le Quéré, C., Luijkx, I. T., Olsen, A., Peters, G. P., Peters, W., Pongratz, J., Schwingshackl, C., Sitch, S., Canadell, J. G., Ciais, P., Jackson, R. B., Alin, S. R., Alkama, R., … Zheng, B. (2022). Global Carbon Budget 2022. Earth System Science Data, 14(11). https://doi.org/10.5194/essd-14-4811-2022

Gaubert, B., Stephens, B. B., Baker, D. F., Basu, S., Bertolacci, M., Bowman, K. W., et al. (2023). Neutral tropical African CO2 exchange estimated from aircraft and satellite observations. Global Biogeochemical Cycles, 37, e2023GB007804. https://doi.org/10.1029/2023GB007804

Gauci, V., Pangala, S. R., Shenkin, A., Barba, J., Bastviken, D., Figueiredo, V., Gomez, C., Enrich-Prast, A., Sayer, E., Stauffer, T., Welch, B., Elias, D., McNamara, N., Allen, M., & Malhi, Y. (2024). Global atmospheric methane uptake by upland tree woody surfaces. *Nature*, *631*(8022), 796–800. https://doi.org/10.1038/s41586-024-07592-w

Goldberg L, Lagomasino D, Thomas N, Fatoyinbo T. (2020). Global declines in human-driven mangrove loss. Glob Change Biol, 26: 5844–5855. https://doi.org/10.1111/gcb.15275

Haider, S., Swain, E., Beerens, J., Petkewich, M., McCloskey, B., and Henkel, H. (2020). The Everglades Depth Estimation Network (EDEN) surface-water interpolation model, version 3: U.S. Geological Survey Scientific Investigations Report 2020–5083, 31 p., https://doi.org/10.3133/sir20205083.

Hao, Q., Liu, F., Zhang, Y., Wang, O., & Xiao, L. (2020). Methylobacter accounts for strong aerobic methane oxidation in the Yellow River Delta with characteristics of a methane sink during the dry season. Science of the Total Environment, 704. https://doi.org/10.1016/j.scitotenv.2019.135383

Hannun, R. A., Wolfe, G. M., Kawa, S. R., Hanisco, T. F., Newman, P. A., Alfieri, J. G., Barrick, J., Clark, K. L., Digangi, J. P., Diskin, G. S., King, J., Kustas, W. P., Mitra, B., Noormets, A., Nowak, J. B., Thornhill, K. L., & Vargas, R. (2020). Spatial heterogeneity in CO2, CH4, and energy fluxes: insights from airborne eddy covariance measurements over the Mid-Atlantic region. Environmental Research Letters, 15(3). https://doi.org/10.1088/1748-9326/ab7391

Harrison, J. A., Deemer, B. R., Birchfield, M. K., & O'Malley, M. T. (2017). Reservoir Water-Level Drawdowns Accelerate and Amplify Methane Emission. Environmental Science and Technology, 51(3). https://doi.org/10.1021/acs.est.6b03185

Hawkes, C. v., Waring, B. G., Rocca, J. D., & Kivlin, S. N. (2017). Historical climate controls soil respiration responses to current soil moisture. Proceedings of the National Academy of Sciences of the United States of America, 114(24). https://doi.org/10.1073/pnas.1620811114

Hayek, M. N., Wehr, R., Longo, M., Hutyra, L. R., Wiedemann, K., Munger, J. W., Bonal, D., Saleska, S. R., Fitzjarrald, D. R., & Wofsy, S. C. (2018). A novel correction for biases in forest eddy covariance carbon balance. Agricultural and Forest Meteorology, 250–251. https://doi.org/10.1016/j.agrformet.2017.12.186

Hayes, D. J., Vargas, R., Alin, S., Conant, R. T., Hutyra, L. R., Jacobson, A. R., Kurz, W. A., Liu, S., McGuire, A. D., Poulter, B., & Woodall, C. W. (2018). The North American Carbon Budget. Second State of the Carbon Cycle Report. Second State of the Carbon Cycle Report (SOCCR2): A Sustained Assessment Report.

Högström, U. (1988). Non-dimensional wind and temperature profiles in the atmospheric surface layer: A re-evaluation. Boundary-Layer Meteorology, 42(1–2). https://doi.org/10.1007/BF00119875

Hondula, K. L., Jones, C. N., & Palmer, M. A. (2021). Effects of seasonal inundation on methane fluxes from forested freshwater wetlands. Environmental Research Letters, 16(8). https://doi.org/10.1088/1748-9326/ac1193

Hutjes, R. W. A., Vellinga, O. S., Gioli, B., & Miglietta, F. (2010). Dis-aggregation of airborne flux measurements using footprint analysis. Agricultural and Forest Meteorology, 150(7–8). https://doi.org/10.1016/j.agrformet.2010.03.004

Iram, N., Kavehei, E., Maher, D. T., Bunn, S. E., Rezaei Rashti, M., Farahani, B. S., & Adame, M. F. (2021). Soil greenhouse gas fluxes from tropical coastal wetlands and alternative agricultural land uses. Biogeosciences, 18(18). https://doi.org/10.5194/bg-18-5085-2021

Jha, C. S., Rodda, S. R., Thumaty, K. C., Raha, A. K., & Dadhwal, V. K. (2014). Eddy covariance based methane flux in Sundarbans mangroves, India. Journal of Earth System Science, 123(5). https://doi.org/10.1007/s12040-014-0451-y

Kljun, N., Calanca, P., Rotach, M. W., & Schmid, H. P. (2015). A simple two-dimensional parameterisation for Flux Footprint Prediction (FFP). Geoscientific Model Development, 8(11). https://doi.org/10.5194/gmd-8-3695-2015

Kljun, N., Rotach, M. W., & Schmid, H. P. (2002). A three-dimensional backward Lagrangian footprint model for a wide range of boundary-layer stratifications. Boundary-Layer Meteorology, 103(2). https://doi.org/10.1023/A:1014556300021

Kristensen, E., Flindt, M. R., Ulomi, S., Borges, A. v., Abril, G., & Bouillon, S. (2008). Emission of CO2 and CH4 to the atmosphere by sediments and open waters in two Tanzanian mangrove forests. Marine Ecology Progress Series, 370. https://doi.org/10.3354/meps07642

Kroeger, K. D., Crooks, S., Moseman-Valtierra, S., & Tang, J. (2017). Restoring tides to reduce methane emissions in impounded wetlands: A new and potent Blue Carbon climate change intervention. Scientific Reports, 7(1). https://doi.org/10.1038/s41598-017-12138-4

Lagomasino, D., Fatoyinbo, T., Castañeda-Moya, E., Cook, B. D., Montesano, P. M., Neigh, C. S. R., Corp, L. A., Ott, L. E., Chavez, S., & Morton, D. C. (2021). Storm surge and ponding explain mangrove dieback in southwest Florida following Hurricane Irma. Nature Communications, 12(1). https://doi.org/10.1038/s41467-021-24253-y

Langford, B., Acton, W., Ammann, C., Valach, A., & Nemitz, E. (2015). Eddy-covariance data with low signal-to-noise ratio: Time-lag determination, uncertainties and limit of detection. Atmospheric Measurement Techniques, 8(10). https://doi.org/10.5194/amt-8-4197-2015

Lee, S. C., Fan, C. J., Wu, Z. Y., & Juang, J. Y. (2015). Investigating effect of environmental controls on dynamics of CO2 budget in a subtropical estuarial marsh wetland ecosystem. Environmental Research Letters, 10(2). https://doi.org/10.1088/1748-9326/10/2/025005

Lenschow, D. H., Mann, J., & Kristensen, L. (1994). How long is long enough when measuring fluxes and other turbulence statistics? Journal of Atmospheric & Oceanic Technology, 11(3). https://doi.org/10.1175/1520-0426(1994)011<0661:HLILEW>2.0.CO;2

Lin, C. W., Kao, Y. C., Chou, M. C., Wu, H. H., Ho, C. W., & Lin, H. J. (2020). Methane emissions from subtropical and tropical mangrove ecosystems in Taiwan. Forests, 11(4). https://doi.org/10.3390/F11040470

Liu, J., & Lai, D. Y. F. (2019). Subtropical mangrove wetland is a stronger carbon dioxide sink in the dry than wet seasons. Agricultural and Forest Meteorology, 278. https://doi.org/10.1016/j.agrformet.2019.107644

Ma, S., Worden, J. R., Bloom, A. A., Zhang, Y., Poulter, B., Cusworth, D. H., Yin, Y., Pandey, S., Maasakkers, J. D., Lu, X., Shen, L., Sheng, J., Frankenberg, C., Miller, C. E., & Jacob, D. J. (2021). Satellite Constraints on the Latitudinal Distribution and Temperature Sensitivity of Wetland Methane Emissions. AGU Advances, 2(3). https://doi.org/10.1029/2021av000408

Macreadie, P. I., Costa, M. D. P., Atwood, T. B., Friess, D. A., Kelleway, J. J., Kennedy, H., Lovelock, C. E., Serrano, O., & Duarte, C. M. (2021). Blue carbon as a natural climate solution. In Nature Reviews Earth and Environment (Vol. 2, Issue 12). https://doi.org/10.1038/s43017-021-00224-1

Malone, S. L., Keough, C., Staudhammer, C. L., Ryan, M. G., Parton, W. J., Olivas, P., Oberbauer, S. F., Schedlbauer, J., & Starr, G. (2015). Ecosystem resistance in the face of climate change: A case study from the freshwater marshes of the Florida Everglades. Ecosphere, 6(4). https://doi.org/10.1890/ES14-00404.1

Marín-Muñiz, J. L., Hernández, M. E., & Moreno-Casasola, P. (2015). Greenhouse gas emissions from coastal freshwater wetlands in Veracruz Mexico: Effect of plant community and seasonal dynamics. Atmospheric Environment, 107. https://doi.org/10.1016/j.atmosenv.2015.02.036

McGowan, H. A., Lowry, A. L., & Gray, M. A. (2020). Identification of Optimum Temperatures for Photosynthetic Production in Subtropical Coastal Ecosystems: Implications for CO2 Sequestration in a Warming World. Journal of Geophysical Research: Biogeosciences, 125(8). https://doi.org/10.1029/2020JG005678

McLeod, E., Chmura, G. L., Bouillon, S., Salm, R., Björk, M., Duarte, C. M., Lovelock, C. E., Schlesinger, W. H., & Silliman, B. R. (2011). A blueprint for blue carbon: Toward an improved understanding of the role of vegetated coastal habitats in sequestering CO2. In Frontiers in Ecology and the Environment (Vol. 9, Issue 10). https://doi.org/10.1890/110004

Megonigal, J. P., & Guenther, A. B. (2008). Methane emissions from upland forest soils and vegetation. Tree Physiology, 28(4). https://doi.org/10.1093/treephys/28.4.491

Melton, J. R., Wania, R., Hodson, E. L., Poulter, B., Ringeval, B., Spahni, R., Bohn, T., Avis, C. A., Beerling, D. J., Chen, G., Eliseev, A. v., Denisov, S. N., Hopcroft, P. O., Lettenmaier, D. P., Riley, W. J., Singarayer, J. S., Subin, Z. M., Tian, H., Zürcher, S., … Kaplan, J. O. (2013). Present state of global wetland extent and wetland methane modelling: Conclusions from a model inter-comparison project (WETCHIMP). Biogeosciences, 10(2). https://doi.org/10.5194/bg-10-753-2013

Moncrieff, J., Clement, R., Finnigan, J., & Meyers, T. (2006). Averaging, Detrending, and Filtering of Eddy Covariance Time Series. In Handbook of Micrometeorology. https://doi.org/10.1007/1-4020-2265-4_2

Murray, N. J., Worthington, T. A., Bunting, P., Duce, S., Hagger, V., Lovelock, C. E., Lucas, R., Saunders, M. I., Sheaves, M., Spalding, M., Waltham, N. J., & Lyons, M. B. (2022). High-resolution mapping of losses and gains of Earth's tidal wetlands. Science, 376(6594). https://doi.org/10.1126/science.abm9583

Murdiyarso, D., Purbopuspito, J., Kauffman, J. B., Warren, M. W., Sasmito, S. D., Donato, D. C., Manuri, S., Krisnawati, H., Taberima, S., & Kurnianto, S. (2015). The potential of Indonesian mangrove forests for global climate change mitigation. Nature Climate Change, 5(12). https://doi.org/10.1038/nclimate2734

Murguia-Flores, F., Jaramillo, V. J., & Gallego-Sala, A. (2023). Assessing Methane Emissions From Tropical Wetlands: Uncertainties From Natural Variability and Drivers at the Global Scale. In Global Biogeochemical Cycles (Vol. 37, Issue 9). https://doi.org/10.1029/2022GB007601

Myneni, R., Knyazikhin, Y., Park, T. (2015). MCD15A2H MODIS/Terra+Aqua Leaf Area Index/FPAR 8-day L4 Global 500m SIN Grid V006 [Data set]. NASA EOSDIS Land Processes Distributed Active Archive Center. Accessed 2024-01-11 from https://doi.org/10.5067/MODIS/MCD15A2H.006

Nahlik, A. M., & Mitsch, W. J. (2011). Methane emissions from tropical freshwater wetlands located in different climatic zones of Costa Rica. Global Change Biology, 17(3). https://doi.org/10.1111/j.1365-2486.2010.02190.x

O'Neill, P. E., S. Chan, E. G. Njoku, T. Jackson, R. Bindlish, J. Chaubell, and A. Colliander. (2023). SMAP Enhanced L3 Radiometer Global and Polar Grid Daily 9 km EASE-Grid Soil Moisture, Version 6 [Data Set]. Boulder, Colorado USA. NASA National Snow and Ice Data Center Distributed Active Archive Center. https://doi.org/10.5067/M20OXIZHY3RJ. Date Accessed 11-11-2023.

Orchard, V. A., & Cook, F. J. (1983). Relationship between soil respiration and soil moisture. Soil Biology and Biochemistry, 15(4). https://doi.org/10.1016/0038-0717(83)90010-X

Pandey, S., Houweling, S., Lorente, A., Borsdorff, T., Tsivlidou, M., Anthony Bloom, A., Poulter, B., Zhang, Z., & Aben, I. (2021). Using satellite data to identify the methane emission controls of South Sudan's wetlands. Biogeosciences, 18(2). https://doi.org/10.5194/bg-18-557-2021

Poulter, B., Adams-Metayer, F. M., Amaral, C., Barenblitt, A., Campbell, A., Charles, S. P., Roman-Cuesta, R. M., D'Ascanio, R., Delaria, E. R., Doughty, C., Fatoyinbo, T., Gewirtzman, J., Hanisco, T. F., Hull, M., Kawa, S. R., Hannun, R., Lagomasino, D., Lait, L., Malone, S. L., … Zhang, Z. (2023). Multi-scale observations of mangrove blue carbon ecosystem fluxes: The NASA Carbon Monitoring System BlueFlux field campaign. *Environmental Research Letters*, *18*(7). https://doi.org/10.1088/1748-9326/acdae6

Rivera-Monroy, V. H., Danielson, T. M., Castañeda-Moya, E., Marx, B. D., Travieso, R., Zhao, X., Gaiser, E. E., & Farfan, L. M. (2019). Long-term demography and stem productivity of Everglades mangrove forests (Florida, USA): Resistance to hurricane disturbance. Forest Ecology and Management, 440. https://doi.org/10.1016/j.foreco.2019.02.036

Rosentreter, J. A., Maher, D. T., Erler, D. v., Murray, R., & Eyre, B. D. (2018a). Factors controlling seasonal CO2 and CH4 emissions in three tropical mangrove-dominated estuaries in Australia. Estuarine, Coastal and Shelf Science, 215. https://doi.org/10.1016/j.ecss.2018.10.003

Rosentreter, J. A., Maher, D. T., Erler, D. v., Murray, R., & Eyre, B. D. (2018b). Seasonal and temporal CO2 dynamics in three tropical mangrove creeks – A revision of global mangrove CO2 emissions. Geochimica et Cosmochimica Acta, 222. https://doi.org/10.1016/j.gca.2017.11.026

Rosentreter, J. A., Maher, D. T., Erler, D. v., Murray, R. H., & Eyre, B. D. (2018c). Methane emissions partially offset "blue carbon" burial in mangroves. Science Advances, 4(6). https://doi.org/10.1126/sciadv.aao4985

Rosentreter, J. A., Borges, A. v., Deemer, B. R., Holgerson, M. A., Liu, S., Song, C., Melack, J., Raymond, P. A., Duarte, C. M., Allen, G. H., Olefeldt, D., Poulter, B., Battin, T. I., & Eyre, B. D. (2021). Half of global methane emissions come from highly variable aquatic ecosystem sources. Nature Geoscience, 14(4). https://doi.org/10.1038/s41561-021-00715-2

Ross, M. S., Ruiz, P. L., Sah, J. P., & Hanan, E. J. (2009). Chilling damage in a changing climate in coastal landscapes of the subtropical zone: A case study from south Florida. Global Change Biology, 15(7). https://doi.org/10.1111/j.1365-2486.2009.01900.x

Ruiz, P. L., A. Lee, C. Thompson, I. Castillo, M. Guichardot, C. P. Perry, A. Arteaga Garcia, M. Foguer, M. C. Prats, E. Garcia, S. Lamosa, R. B. Shamblin, and K. R. T. Whelan. (2019). The Everglades National Park and Big Cypress National Preserve vegetation mapping project: Interim report—Eastern Big Cypress (Regions 5 & 6), Big Cypress National Preserve. Natural Resource Report NPS/SFCN/NRR—2019/2035. National Park Service, Fort Collins, Colorado.

Ruiz, P. L., T. N. Schall, R. B. Shamblin, and K. R. T. Whelan. (2021). The vegetation of Everglades National Park: Final report. Natural Resource Report NPS/SFCN/NRR—2021/2256. National Park Service, Fort Collins, Colorado. https://doi.org/10.36967/nrr-2286460.

Sanderman, J., Hengl, T., Fiske, G., Solvik, K., Adame, M. F., Benson, L., Bukoski, J. J., Carnell, P., Cifuentes-Jara, M., Donato, D., Duncan, C., Eid, E. M., Ermgassen, P. Z., Lewis, C. J. E., Macreadie, P. I., Glass, L., Gress, S., Jardine, S. L., Jones, T. G., … Landis, E. (2018). A global map of mangrove forest soil carbon at 30 m spatial resolution. Environmental Research Letters, 13(5). https://doi.org/10.1088/1748-9326/aabe1c

Saunois, M., R. Stavert, A., Poulter, B., Bousquet, P., G. Canadell, J., B. Jackson, R., A. Raymond, P., J. Dlugokencky, E., Houweling, S., K. Patra, P., Ciais, P., K. Arora, V., Bastviken, D., Bergamaschi, P., R. Blake, D., Brailsford, G., Bruhwiler, L., M. Carlson, K., Carrol, M., … Zhuang, Q. (2020). The global methane budget 2000-2017. Earth System Science Data, 12(3). https://doi.org/10.5194/essd-12-1561-2020

Schedlbauer, J. L., Munyon, J. W., Oberbauer, S. F., Gaiser, E. E., & Starr, G. (2012). Controls on ecosystem carbon dioxide exchange in short- and long-hydroperiod Florida everglades freshwater marshes. Wetlands, 32(5). https://doi.org/10.1007/s13157-012-0311-y

Schiferl, L. D., Watts, J. D., Larson, E. J. L., Arndt, K. A., Biraud, S. C., Euskirchen, E. S., Goodrich, J. P., Henderson, J. M., Kalhori, A., Mckain, K., Mountain, M. E., Munger, J. W., Oechel, W. C., Sweeney, C., Yi, Y., Zona, D., & Commane, R. (2022). Using atmospheric observations to quantify annual biogenic carbon dioxide fluxes on the Alaska North Slope. Biogeosciences, 19(24). https://doi.org/10.5194/bg-19-5953-2022

Sellers, P. J., Hall, F. G., Kelly, R. D., Black, A., Baldocchi, D., Berry, J., Ryan, M., Ranson, K. J., Crill, P. M., Lettenmaier, D. P., Margolis, H., Cihlar, J., Newcomer, J., Fitzjarrald, D., Jarvis, P. G., Gower, S. T., Halliwell, D., Williams, D., Goodison, B., … Guertin, F. E. (1997). BOREAS in 1997: Experiment overview, scientific results, and future directions. Journal of Geophysical Research Atmospheres, 102(24). https://doi.org/10.1029/97jd03300

Shaw, J. T., Allen, G., Barker, P., Pitt, J. R., Pasternak, D., Bauguitte, S. J.-B., et al. (2022). Large methane emission fluxes observed from tropical wetlands in Zambia. Global Biogeochemical Cycles, 36, e2021GB007261. https://doi.org/10.1029/2021GB007261

Shoemaker, W. B., Anderson, F., Barr, J. G., Graham, S. L., & Botkin, D. B. (2015). Carbon exchange between the atmosphere and subtropical forested cypress and pine wetlands. Biogeosciences, 12(8). https://doi.org/10.5194/bg-12-2285-2015

Simard, M., Fatoyinbo, L., Smetanka, C., Rivera-Monroy, V. H., Castañeda-Moya, E., Thomas, N., & van der Stocken, T. (2019). Mangrove canopy height globally related to precipitation, temperature and cyclone frequency. Nature Geoscience, 12(1). https://doi.org/10.1038/s41561-018-0279-1

Smith, T. J., Anderson, G. H., Balentine, K., Tiling, G., Ward, G. A., & Whelan, K. R. T. (2009). Cumulative impacts of hurricanes on Florida mangrove ecosystems: Sediment deposition, storm surges and vegetation. Wetlands, 29(1). https://doi.org/10.1672/08-40.1

Souza, R. B., Copertino, M. S., Fisch, G., Santini, M. F., Pinaya, W. H. D., Furlan, F. M., Alves, R. de C. M., Möller, O. O., & Pezzi, L. P. (2022). Salt marsh-atmosphere CO2 exchanges in Patos Lagoon Estuary, Southern Brazil. *Frontiers in Marine Science*, *9*. https://doi.org/10.3389/fmars.2022.892857

Taillie, P. J., Roman-Cuesta, R., Lagomasino, D., Cifuentes-Jara, M., Fatoyinbo, T., Ott, L. E., & Poulter, B. (2020). Widespread mangrove damage resulting from the 2017 Atlantic mega hurricane season. Environmental Research Letters, 15(6). https://doi.org/10.1088/1748-9326/ab82cf

Torrence, C., & Compo, G. P. (1998). A Practical Guide to Wavelet Analysis. Bulletin of the American Meteorological Society, 79(1). https://doi.org/10.1175/1520-0477(1998)079<0061:APGTWA>2.0.CO;2

Troxler, T. G., Gaiser, E., Barr, J., Fuentes, J. D., Jaffé, R., Childers, D. L., Colado-Vides, L., Rivera-Monroy, V. H., Castañeda-Moya, E., Anderson, W., Chambers, R., Chen, M., Coronado-Molina, C., Davis, S. E., Engel, V., Fitz, C., Fourqurean, J., Frankovich, T., Kominoski, J., Madden C., Malone S., Oberbauer S., Olivas P., Richards J., Saunders C., Schedlbauer J., Scinto L., Sklar F., Smith T., Smoak J., Starr G., Twilley R., Whelan, K. (2013). Integrated carbon budget models for the everglades terrestrial-coastal-oceanic gradient: Current status and needs for inter-site comparisons. Oceanography, 26(3). https://doi.org/10.5670/oceanog.2013.51

Troxler, T. G., Barr, J. G., Fuentes, J. D., Engel, V., Anderson, G., Sanchez, C., Lagomasino, D., Price, R., & Davis, S. E. (2015). Component-specific dynamics of riverine mangrove CO2 efflux in the Florida coastal Everglades. Agricultural and Forest Meteorology, 213. https://doi.org/10.1016/j.agrformet.2014.12.012

Wang, J. S., Randolph Kawa, S., James Collatz, G., Sasakawa, M., Gatti, L. v., Machida, T., Liu, Y., & Manyin, M. E. (2018). A global synthesis inversion analysis of recent variability in CO2 fluxes using GOSAT and in situ observations. Atmospheric Chemistry and Physics, 18(15). https://doi.org/10.5194/acp-18-11097-2018

Whelan, K. R. T., M. Prats, and A. J. Atkinson. (2020). Western Big Cypress National Preserve vegetation map. Natural Resource Report NPS/SFCN/NRR—2020/2170. National Park Service, Fort Collins, Colorado. https://doi.org/10.36967/nrr-2278240.

Wolfe, G. M., Hanisco, T. F., Arkinson, H. L., Bui, T. P., Crounse, J. D., Dean-Day, J., Goldstein, A., Guenther, A., Hall, S. R., Huey, G., et al. (2015), Quantifying sources and sinks of reactive gases in the lower atmosphere using airborne flux observations, *Geophys. Res. Lett*., 42, 8231–8240, doi:10.1002/2015GL065839.

Wolfe, G. M., Kawa, S. R., Hanisco, T. F., Hannun, R. A., Newman, P. A., Swanson, A., Bailey, S., Barrick, J., Thornhill, K. L., Diskin, G., DiGangi, J., Nowak, J. B., Sorenson, C., Bland, G., Yungel, J. K., and Swenson, C. A. (2018). The NASA Carbon Airborne Flux Experiment (CARAFE): instrumentation and methodology, *Atmos. Meas. Tech*., 11, 1757–1776, https://doi.org/10.5194/amt-11-1757-2018

Xiong, L., Lagomasino, D., Charles, S. P., Castañeda-Moya, E., Cook, B. D., Redwine, J., & Fatoyinbo, L. (2022). Quantifying mangrove canopy regrowth and recovery after Hurricane Irma with large-scale repeat airborne lidar in the Florida Everglades. International Journal of Applied Earth Observation and Geoinformation, 114. https://doi.org/10.1016/j.jag.2022.103031

Zhang, Z., Poulter, B., Feldman, A. F., Ying, Q., Ciais, P., Peng, S., & Li, X. (2023). Recent intensification of wetland methane feedback. Nature Climate Change, 13(5). https://doi.org/10.1038/s41558-023-01629-0

Zhao, J., S. L. Malone, C. L. Staudhammer, G. Starr, H. Hartmann, S. F. Oberbauer (2021). Wetland plants respond nonlinearly to inundation over a sustained period. American Journal of Botany.108, 1917-1931.

Zhu, X., Qin, Z., & Song, L. (2021). How Land-Sea Interaction of Tidal and Sea Breeze Activity Affect Mangrove Net Ecosystem Exchange? Journal of Geophysical Research: Atmospheres, 126(8). https://doi.org/10.1029/2020JD034047

Zulueta, R. C., Oechel, W. C., Verfaillie, J. G., Hastings, S. J., Gioli, B., Lawrence, W. T., & Paw U, K. T. (2013). Aircraft regional-scale flux measurements over complex landscapes of Mangroves, desert, and marine ecosystems of Magdalena Bay, Mexico. Journal of Atmospheric and Oceanic Technology, 30(7). https://doi.org/10.1175/JTECH-D-12-00022.1